UC Riverside
UC Riverside Electronic Theses and Dissertations

Title

Non Equilibrium Current Activated Pressure Assisted Densification Processing of Aluminum Nitride Doped with Rare Earths for Laser Applications

Permalink

Author

Wieg, Andrew Thomas

Publication Date

2015

Peer reviewed|Thesis/dissertation

UNIVERSITY OF CALIFORNIA
RIVERSIDE

Non Equilibrium Current Activated Pressure Assisted Densification
Processing of Aluminum Nitride Doped with Rare Earths for Laser Applications

A Dissertation submitted in partial satisfaction
of the requirements for the degree of

Doctor of Philosophy

in

Mechanical Engineering

by

Andrew Thomas Wieg

March 2015

Dissertation Committee
        Dr. Javier E. Garay, Chairperson
        Dr. Lorenzo Mangolini
        Dr. Elaine Haberer

The Dissertation of Andrew Thomas Wieg is approved:

_____

_____

_____

Committee Chairperson

University of California, Riverside

Acknowledgements

ABSTRACT OF THE DISSERTATION

Non Equilibrium Current Activated Pressure Assisted Densification
Processing of Aluminum Nitride Doped with Rare Earths for Laser Applications

by

Andrew Thomas Wieg

Doctor of Philosophy, Graduate Program in Mechanical Engineering
University of California, Riverside, March 2015
Dr. Javier E. Garay, Chairperson

The performance of Solid State lasers and solid state lighting have long suffered from thermal management difficulties. Thermal management continues to be one of the major challenges in the development of high powered light sources such as solid state lasers. In particular, the low thermal conductivity of standard photoluminescent (PL) host materials limits the overall power output and/or duty cycle. Overheating in laser host materials can lead to performance issues and ultimately irreparable failure. One significant problem is the materials ability to tolerate thermal shock and the stresses caused by thermal gradients. A material with high thermal conductivity will be able to dissipate more heat while maintaining a smaller thermal gradient, thus reducing the degradation of performance from thermal effects such as thermal lensing and thermally induced fracture. Aluminum Nitride's wide band gap and high thermal conductivity offer the potential to improve some of these problems. In this dissertation the author presents research conducted on the processing and doping of Aluminum Nitride for photoluminescent and solid state laser applications. Areas discussed include, non equilibrium CAPAD processing of doped and undoped AlN, doping of AlN for visible and infrared emission and thermomechanical properties of doped AlN

Table of Contents

List of Figures

Schematic description of a laser rod with pumping and water cooling (a) and the thermal

gradients within a laser rod with external water cooling under thermal load from

pumping. Significant temperature gradients can lead to problems including broken parts.

Simulation of the influence of thermal conductivity on thermal gradients in laser rods

under thermal load from pumping. (a) shows the simulated temperature gradient for

Nd:YAG in comparison with (b) Tb:AlN. Increasing thermal conductivity clearly allows

much more aggressive pumping for the same thermal gradient and thermal stresses. The

temperature gradient in Nd:YAG easily exceeds 100 °C. [53]

Energy level diagrams for (a) three and (b) four level laser systems typical of ruby and

rare earth ions in glass or crystalline hosts respectively. Four level lasers tend to be more

efficient, which is part of why doping with rare earth ions has been so successful.

Examples of progress in Nd:YAG ceramics developed by Ikesue and others. [45]

List of Tables

1. Introduction and motivation

Scientific research is often driven by a problem with existing technology, and this project is no exception. Solid state lighting and lasers are seeing an ever wider range of uses and laser materials have seen near constant development efforts since the early 1960s. Thermal management has long been a problem in high power photonic devices, including solid state lighting and high power lasers. Despite recent advances in high power solid state lighting and solid state lasers, waste heat still presents a significant problem. One of the main problems, especially from a materials engineering perspective, is the low thermal conductivity of state of the art photoluminescent (PL) materials.
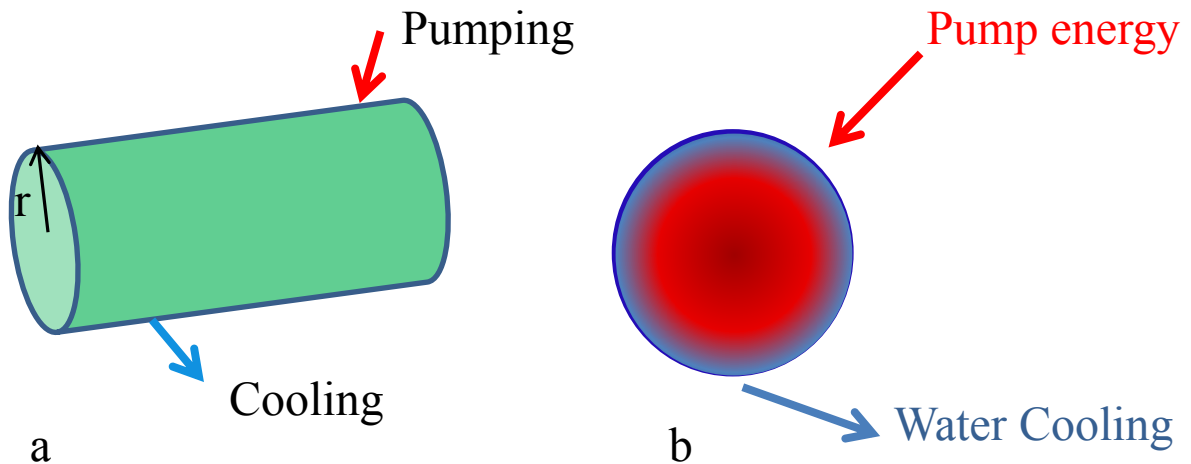
Figure 1.1 Schematic description of a laser rod with pumping and water cooling (a) and the thermal gradients within a laser rod with external water cooling under thermal load from pumping. Significant temperature gradients can lead to problems including broken parts.

Figure 1.1 schematically describes thermal loading and cooling in a laser gain rod under optical pumping. The resulting thermal gradients lead to significant stresses, which under aggressive pumping can lead to gain media fracture. **Figure 1.2** schematically

describes the possible reduction in thermal gradient and thus thermally induced stress by

increasing the thermal conductivity of the laser gain media. By carefully selecting and

processing potential optical gain media materials, the opportunity exists for significant

improvements. Application of these improvements could significantly improve

technologies.
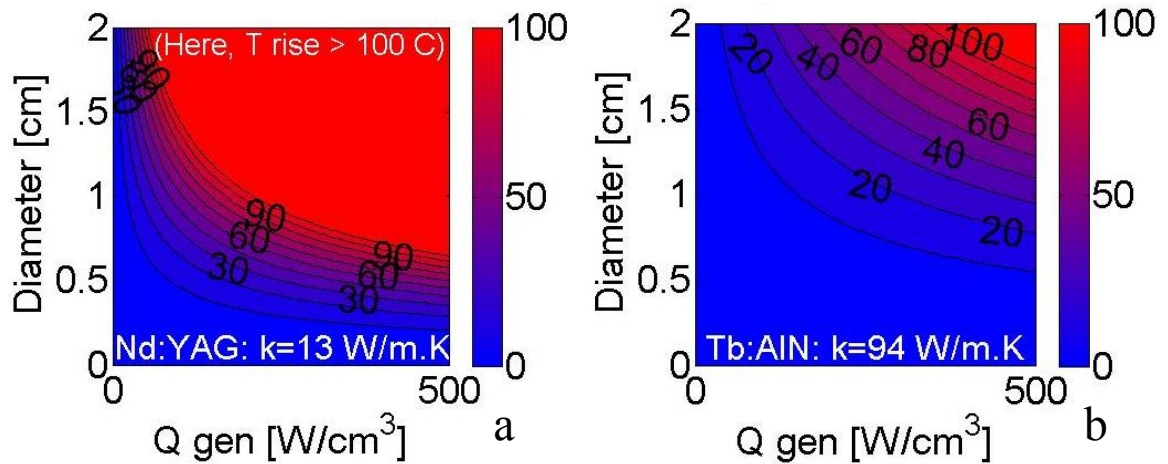
Figure 1.2 Simulation of the influence of thermal conductivity on thermal gradients in laser rods under thermal load from pumping. (a) shows the simulated temperature gradient for Nd:YAG in comparison with (b) Tb:AlN. Increasing thermal conductivity clearly allows much more aggressive pumping for the same thermal gradient and thermal stresses. The temperature gradient in Nd:YAG easily exceeds 100 °C. [53]

2 Background

2.1 Laser background

Solid state lasers all have several characteristics in common including the gain media, an energy source (often referred to as a pump source) and some other optical components depending of the design of the laser. One very common design for a laser involves a set of two mirrors that form an optical cavity in which the light amplifier can resonate. The pump source is often a flash lamp or a laser diode that produces the appropriate wavelength, that when absorbed by active ions in the laser gain media, excites electrons in the active ions to an energy state above their ground state. When more of the active ions have been excited than those remaining at the ground state, a population inversion has been created. These excited electrons can then either spontaneously or due to some stimulation, return to their ground state releasing some waste heat and a photon. This process usually occurs through either a three or four level process as described schematically in **Figure 2.1**

Emission of photons can be stimulated by interaction with electromagnetic radiation, such as light passing through the material. When a population inversion is created in an optical gain material that has been placed in an optical cavity, light bouncing back and forth between the two mirrors can stimulate emission from the excited ions. This creates amplification of light through stimulated emission.
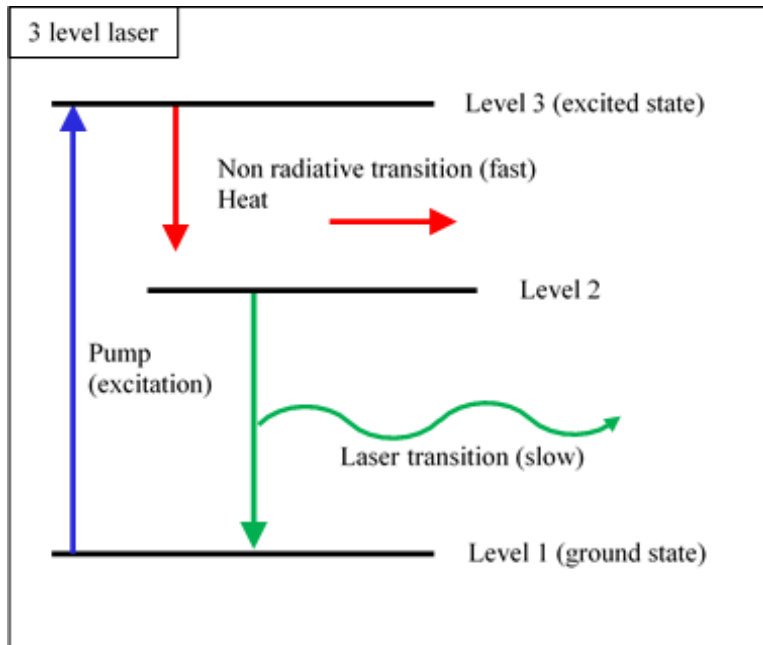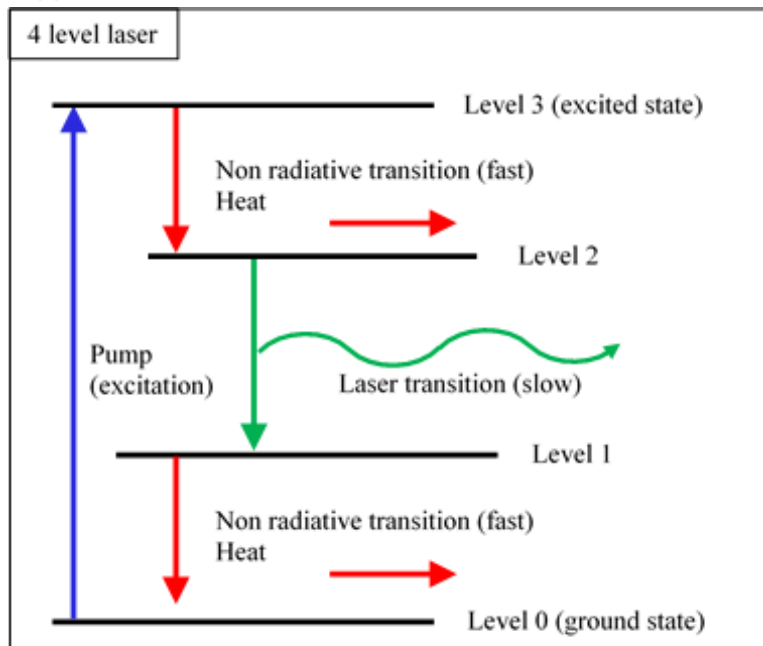
Figure 2.1 Schematic description of energy level diagrams for (a) three and (b) four level laser systems typical of ruby and rare earth ions in glass or crystalline hosts respectively. Four level lasers tend to be more efficient, which is part of why doping with rare earth ions has been so successful.

The first successful solid state laser was demonstrated by T. Maiman in 1960 at Hughes Aircraft, using ruby as the laser host material and coating the ends of the cylinder to create mirrors. The ruby was then excited using a flash lamp. [1] Maiman's research was followed quickly by the development of a wide variety of lasers. By 1964, J.E Guesic and coworkers at Bell labs had developed the first neodymium doped yttrium aluminum garnet (Nd:YAG) based laser. The neodymium ions absorb 808 nm light and emit 1064 nm light. With extensive development efforts solid state lasers and laser materials progressed quickly, however producing large high quality uniformly doped single crystals has proven to be very difficult and time intensive.

2.2 Laser materials background

Because of the size, doping uniformity and structural limitations imposed by single crystal laser hosts (typically grown from a melt), significant development efforts have been focused on polycrystalline laser host materials. Initial efforts proved less than satisfactory due to the difficulty in eliminating pores and defects from optical ceramics. In 1995 Ikesue showed that pressure plays an important role in reducing the number of pores in an optical ceramic, thus decreasing the number of scattering sites and improving optical quality. [41] By carefully controlling of the processing parameters Ikesue and coworkers have been able to produce polycrystalline Nd:YAG with very clean high quality microstructure and very few scattering sites. [41-43] Also because the production of optical ceramics typically does not involve melting, Ikesue has reported much higher dopant concentrations than what is possible in conventionally produced single crystal Nd:YAG [44].

Figure 2.2 shows some of the doped YAG ceramics that have become possible because of these advances in processing [45]. These advances are very promising and impressive. However despite the very impressive processing and microstructural control shown by Ikesue and others, leading to very high optical quality. The performance of YAG based solid state lasers is limited by the ability of the material to dissipate waste heat quickly. This inability to transfer heat quickly limits the power output in order to avoid developing a large thermal gradient which can lead to stresses high enough to fracture the gain media. It is also important to remember that the examples shown in **Figure 2.2** have a cubic crystal structure, eliminating the difficulties associated with birefringent materials.
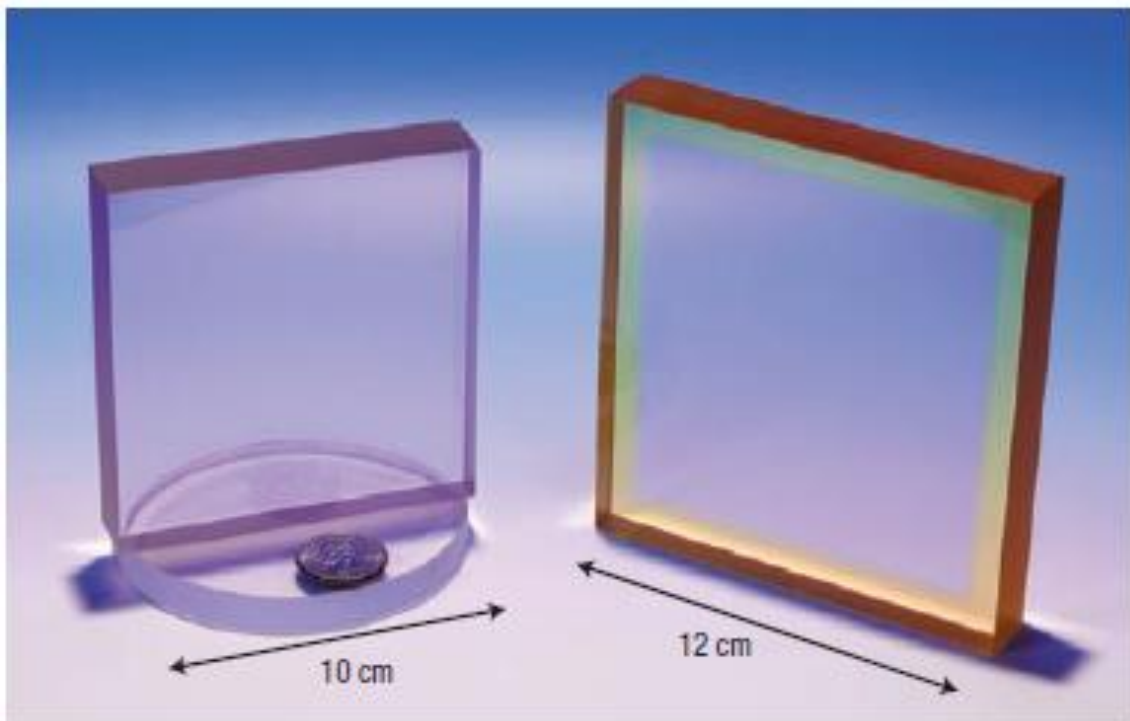
Figure 2.2. Examples of progress in cubic Nd:YAG ceramics developed by Ikesue and others . [45]

As discussed in [52], in polycrystalline materials with randomly oriented grains, with each grain having an anisotropic index of refraction, birefringence presents a significant challenge to obtaining a highly transparent material. Examples of materials where this problem presents significant challenges include alumina and aluminum nitride. Both of these materials are desirable potential host materials for potential performance improvements in solid state lasers. One approach to minimizing the influence of birefringence is reducing the grain size of the material to below the wavelength of light, thus reducing the scattering from birefringence.

Thermal management can be approached from several directions including materials selection and materials design. The performance of these devices could potentially be improved significantly by the development of a robust high thermal conductivity PL material. The group III nitrides and in particular Aluminum Nitride (AlN) are known to be wide bandgap (6.2 eV) semiconductors with high thermal conductivity (300 $Wm^{-1}K^{-1}$ theoretical value)[46,4]. Because of these properties researchers have had a long standing interest in processing and characterizing aluminum nitride. If aluminum nitride can be successfully processed to obtain high optical quality while being doped with rare earth ions (RE) and maintain even a fraction of its theoretical thermal conductivity, significant improvements should be available. Aluminum nitride also offers several unique challenges including birefringence and low equilibrium dopant solubility.[5,6,32]

To further illustrate the improvement in thermal management available from increased thermal conductivity in a laser host material, the steady state radial temperature compared to normalized radius in a cylindrical gain material under water cooling at the surface with volume heat generation from pumping was plotted in **Figure 2.3**. The radial temperature T(r) as described in [40] is given by equation 1 where K is the thermal conductivity, Q is the heat generated per unit volume, r_0 is the radius of the rod. Q is given by equation 3 where P_h is the total heat dissipated and l is the length of the rod. Equation 4 describes the temperature difference between the outer surface of the gain media and the coolant where T_F is the coolant temperature, A is the surface area and h is the surface heat transfer coefficient.

$$T(r) = T(r_0) + \left(\frac{Q}{4K}\right)(r_0^2 - r^2) \qquad \text{Eq.1}$$

$$P_h = 2\pi r_0 lh[T(r_0) - T_F] \qquad \text{Eq.2}$$

$$Q = \frac{P_h}{\pi r_0^2 l} \qquad \text{Eq.3}$$

$$T(r_0) - T_F = \frac{P_h}{Ah} \qquad \text{Eq.4}$$
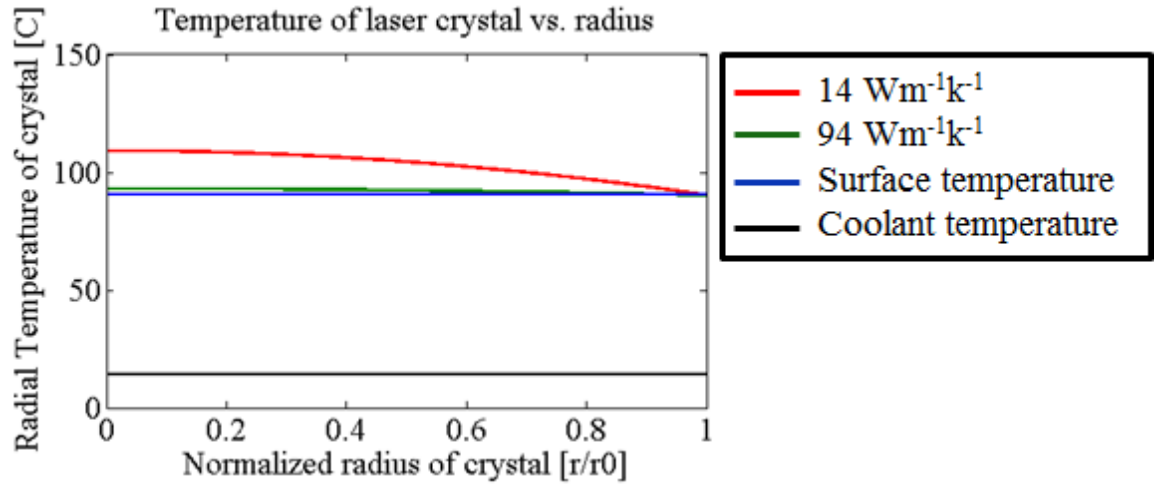
Figure 2.3 Comparison of radial temperature gradients under a given pump power for a cylindrical gain media with thermal conductivities of 14 Wm⁻¹k⁻¹ (red) and 94 Wm⁻¹k⁻¹ (green). As expected, with higher thermal conductivity, a material could be pumped much more aggressively under the same cooling scheme due to the reduced thermally induced stresses.

One method of comparing the thermal loading tolerance of different materials has been described by Koechner and coworkers in [40], as the thermal shock resistance figure of merit R_s where

$$R_S = \frac{k(1-v)}{\alpha E} \sigma_f \left(\frac{w}{m}\right)$$

Eq. 5

This figure of merit allows comparisons to be made between different materials by combining both thermal and mechanical properties into one number describing the thermal loading tolerance of a material.

2.3 AlN historical background

A large portion of this interest in AlN stems from its attractive properties. These properties include a large band gap 6.15 eV [10] and high thermal conductivity [30]. Many of the early studies on aluminum nitride, including the growth of single crystals, thermal conductivity measurements and measuring optical properties including birefringence were conducted between the late 1950s and the 1970s. Some of the early AlN crystals were grown by Matsumura and coworkers and examples of these can be seen in [31]. The thermal conductivity of Aluminum Nitride was also measured a little while later as reported by Borom and coworkers in [30]. Examples of some early AlN single crystal samples grown by Matsumura and coworkers can be seen in **Figure 2.4** [31].

2.4 AlN optical properties background

Some of the earliest optical measurements on aluminum nitride were conducted shortly after initial techniques for producing single crystal aluminum nitride were developed. Matsumura and Tanabe reported on two techniques (Frerichs' method and Sublimation method) and reported the products including rod like crystals [31]. G.A. Cox and coworkers also reported on the synthesis of single crystal aluminum nitride using a sublimation approach [21]. In the same paper they also report on the optical absorbance and some electrical properties of the AlN single crystals they grew. It was observed by [21] that the "optical absorbance" was effected by both annealing and nitrogen vacancy concentration. Other factors are also known to affect the optical behavior of AlN.

Because of aluminum nitrides hexagonal (2h) structure, with lattice parameters (a~3.11A, c~4.98A)[37], birefringence is a common problem for AlN in polycrystalline optical applications. The index of refraction has been reported as "$n_0 = 2.17 \pm 0.05$ and $n_e = 2.22 \pm 0.05$" [32]. Because of this birefringence, polycrystalline aluminum nitride has been very difficult to process to transparency. Nearly all reports of translucent or transparent AlN required the use of sintering additives, including the examples of previous work by Xiong and coworkers in **Figure 2.5**.
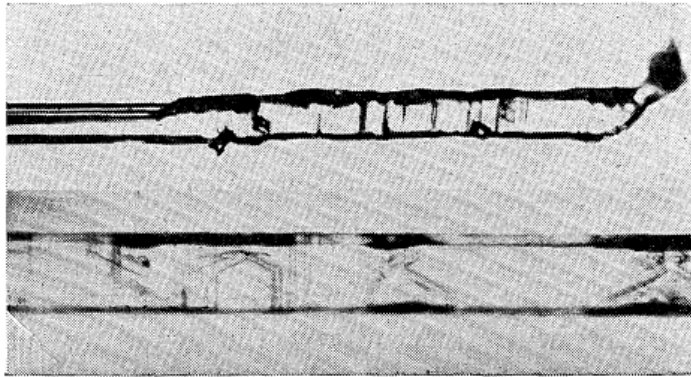
Photo. 1.   Rod-like crystals.
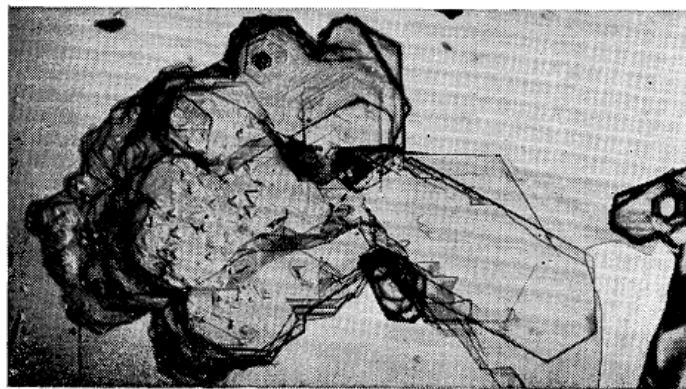
Photo. 2.   Plate-like crystal.

Figure 2.4 Examples of some of the first AlN single crystals grown by Matsumura and coworkers. [31]
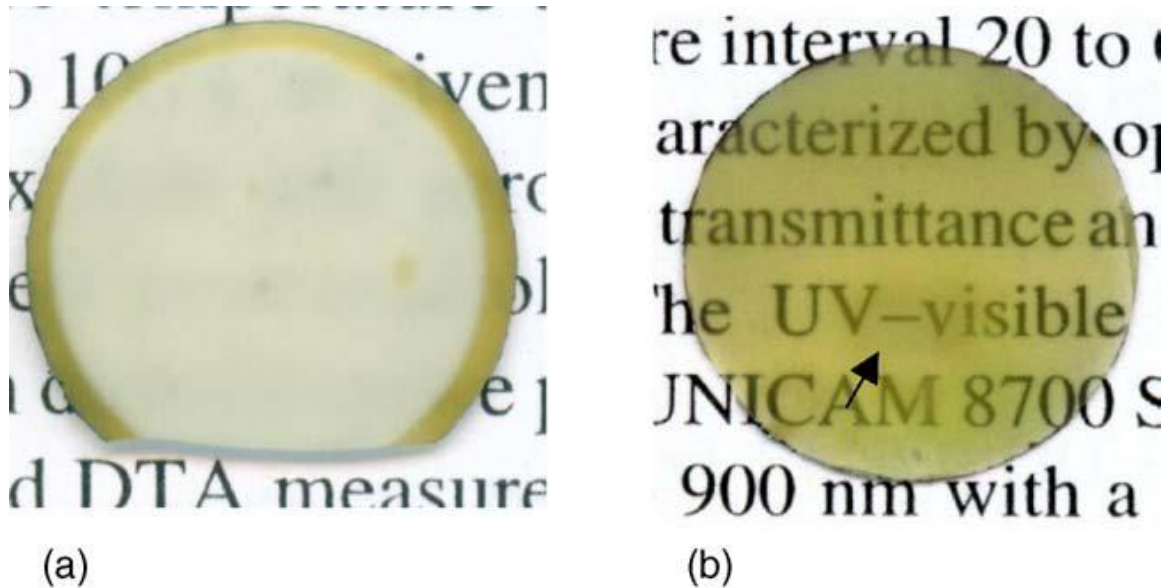
Figure 2.5 Polycrystalline AlN samples produced by Xiong and coworkers, (a) without and (b) with sintering additives. In this case, sintering additives were needed to obtain desirable results [51].

2.5 AlN Thermal properties background

One of the most attractive properties of aluminum nitride is its high thermal conductivity. This high thermal conductivity in combination with a wide bandgap and electrically insulating behavior are very desirable for many applications. Historically, processing of AlN for high thermal conductivity has proven similarly difficult to processing for optical applications. Despite the theoretically high thermal conductivity afforded by aluminum nitride, the thermal conductivity of AlN is easily degraded by contamination. Unfortunately, even with careful processing it is all too easy to degrade this high thermal conductivity. It has been known for some time, that as reported by [30] there is a significant difference between the theoretical thermal conductivity of AlN and the thermal conductivity of commercially available aluminum nitride. It is also well

12

known as discussed by Slack and coworkers in [4] that even small amounts of oxygen contamination can significantly reduce the thermal conductivity of AlN.

Even though it is very easy to degrade the thermal conductivity of AlN with less than ideal processing, oxide ceramics are often even more limited by their thermal conductivity. For example neodymium doped yttrium aluminum garnet (Nd:YAG) has a thermal conductivity k of 14 W/(m•K) [3], and even the lowest reported values for the thermal conductivity of AlN are significantly higher. Single crystal AlN has been reported to have a theoretical k value of 320 W/(m•K) [4].

2.6 AlN photoluminescent background

Beginning with the development of the ruby laser [1], single crystal oxide materials have become very desirable for a large number of solid state light emission applications including solid state lasers. More recently polycrystalline oxide ceramics have seen significant development, some to the point of rivaling their single crystal competitors [2]. The future for polycrystalline PL materials appears promising, especially for scalability and uniformity considerations. Light emission from both doped and undoped AlN, especially in easier to make and dope thin films has been studied extensively in both the photoluminescent (PL) and cathodoluminescent (CL) regimes. Several early descriptions of luminescence in AlN include [29,33,34]. As early as 1966, [33] described both PL and CL from Mn:AlN. Part of why most doping studies in AlN have been conducted using non equilibrium thin film techniques is the low equilibrium solubility of large RE ions in the AlN lattice[5,6]. Luminescence from oxygen impurities was also reported and characterized by [34]. Because aluminum nitride has a wide band gap (6.15 eV) [10], if

13

doping with rare earth (RE) metals is successful, emission over a broad range of the visible spectrum should be possible. The processing required to incorporate active RE ions into the aluminum nitride lattice, poses significant challenges because of the low solubility of rare earths in AlN, usually less than 0.1% [5,6].

This low solubility is at least partially caused by the significant difference in ionic radii between aluminum and many RE elements. For example, assuming that the RE atom will substitute onto an aluminum site and taking as an example terbium, the Tb^{3+} ions are 0.52 Å larger than the atom they would replace (0.57Å vs 1.09Å) ionic radii for aluminum and terbium respectively. Because of this equilibrium processing techniques have been unable to successfully incorporate sufficient quantities of RE elements into AlN and previous researchers have turned to non-equilibrium thin film processing approaches.

Non equilibrium techniques have been more successful. One of these techniques is thin film ion implantation, which has been studied significantly in group 3 nitride thin films for optoelectronic applications [7-11]. While ion implantation shows promise in thin film applications, it is limited to short distances below the surface of the sample, usually less than 1 μm. Because of this another non-equilibrium processing approach is needed for bulk polycrystalline ceramics. One such non-equilibrium processing technique is current activated pressure assisted densification (CAPAD), this processing approach is commonly referred to as spark plasma sintering (SPS). The following will describe the experimental procedures used in the application of this processing technique to consolidation and doping of bulk polycrystalline AlN, and the results observed.

3.0 Experimental procedure

3.1 Powder Processing

All samples discussed in this paper were processed from commercially available aluminum nitride (97% purity as AlN, 1–2 μm size, Tokuyama co, Japan) and rare earth powders (99.9% purity (REO) 40 mesh Tb powder, Alfa Aesar, 99.9% purity (REO) 200 mesh Nd powder, Alfa Aesar) using Current Activated Pressure Assisted Densification (CAPAD). The samples discussed here were made from powders in three different conditions: as-received powders, low energy ball milled (LEBM) powders, and powders milled with high energy planetary ball milling (HEBM). Dopant powders were used in two different conditions, as received and RE nitride powders. In both cases, the powders were mixed using milling. For HEBM, AlN and dopant powders were planetary ball milled under argon using a Fritsch Pulverisette 7 premium line. The high energy milling parameters were ball:powder mass ratio of 10:1, at 450 rpm or 600 rpm for 3 h. Either pure Tb, TbN or NdN was used as a dopant source. In order to synthesize TbN and NdN, Tb powder or Nd powder was nitrided in a tube furnace at 600 ℃ for 6 h under flowing nitrogen. The RE powders were loaded into the furnace tube under an argon atmosphere and sealed before transfer to the furnace, initiating nitrogen flow and subsequent heating. The dopant concentrations, dopant source and ball milling method are available for each sample in **Table 1** (Tb doped) **Table 2** (Nd doped).

Sample	Dopant	CAPAD temperature (°C)
1	none	1700
2	0.25Tb(H)	1700
3	0.25TbN(H)	1700
4	0.5TbN(H)	1700
5	0.5TbN(L)	1700
Coorstek AlN 170	Commercial	Commercial
1.1Nd:YAG	1.1 Nd	Commercial

Table 1 Summary of doping and processing parameters for Tb doped aluminum nitride samples (this work) and commercial samples (measured for comparison) presented here. High energy planetary ball milling and milling rpm are indicated by (H) while low energy ball milling is indicated by (L).

Sample	Dopant	CAPAD temperature (°C)
Nd-1	0.5Nd(H:450)	1700
Nd-2	0.5Nd(H:450)	1700
Nd-3	0.5Nd(H:450)	1700
Nd-4	0.5Nd(H:450)	1700
Nd-5	0.5Nd(H:450)	1700
Nd-6	0.5Nd(H:600)	1750

Table 2. Summary of doping, milling and CAPAD processing parameters for Nd doped AlN samples presented. High energy planetary ball milling and milling rpm are indicated by (H:rpm) and low energy ball milling is indicated by (L).

3.2 CAPAD Processing

For consolidation using the CAPAD process, powders were loaded into a graphite die and plunger set under argon atmosphere in an inert atmosphere glovebox. The die and plunger assembly was then loaded into the CAPAD device. Once the sample was in the CAPAD apparatus, mechanical vacuum was pulled before processing took place. Densification was conducted using 105 MPa of applied pressure and a heating rate of approximately 500°C per minute. Maximum hold temperature was 1800°C, and the processing times were less than 18 minutes. The CAPAD apparatus is schematically described in **Figure 3.1**
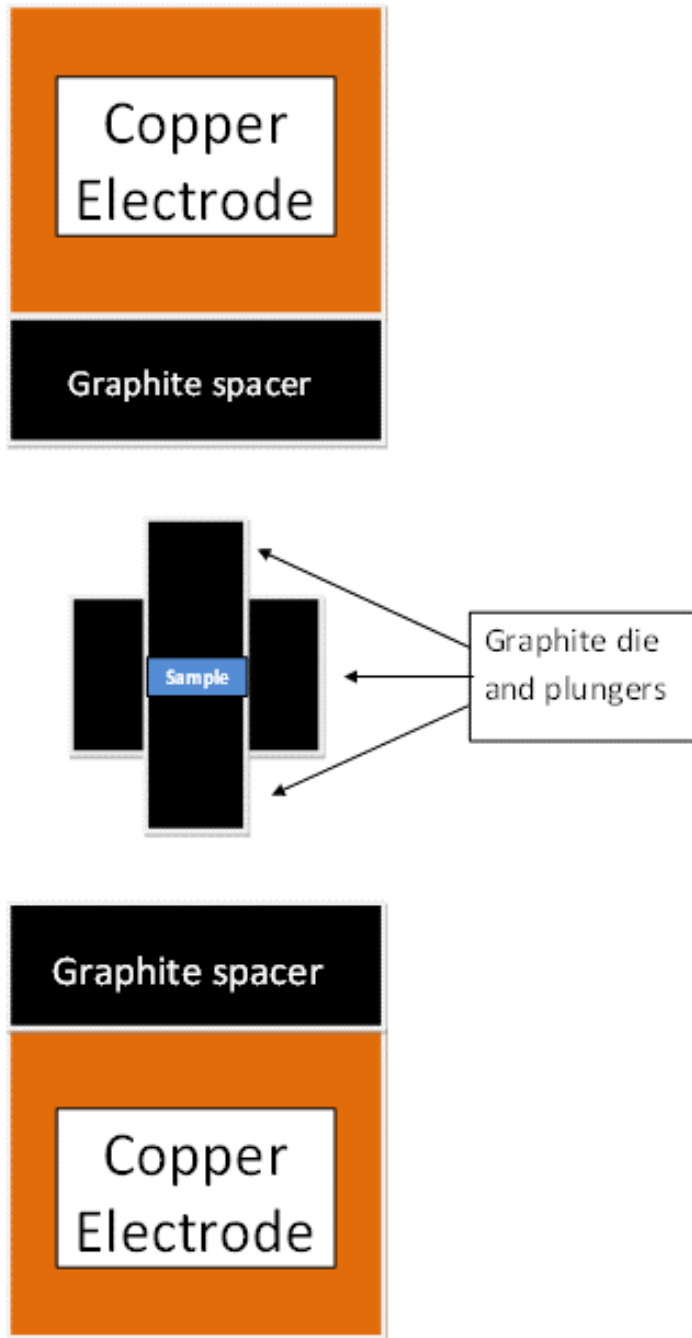
Figure 3.1 Schematic description of the CAPAD apparatus, showing a cross sectional view of a graphite die and plunger assembly with a sample in the center. Load and current are applied through copper electrodes which are protected by graphite spacers. This assembly is surrounded by a vacuum chamber during processing.

3.3 Microstructural characterization

The relative density of the samples was measured using the Archimedes method. The microstructure of the samples was characterized using a Phillips FEG30 scanning electron microscope (SEM) with both secondary (SE) and back scatter electron (BSE) detectors for topography and phase distribution respectively. Samples were also characterized for phase using a Bruker D8 Advance XRD with copper Kα radiation. Samples were characterized for grain size by measuring individual grains on SEM micrographs using ImageJ. The results reported are averages of at least 100 grain measurements except where noted. In order to characterize the microstructural uniformity within each sample and between samples, a set of 3 samples was produced and each sample was examined under SEM using both SE and BSE detectors. Micrographs were taken at 6 spots on each sample and the spots were arranged in a grid as is schematically described in **Figure 3.2**.
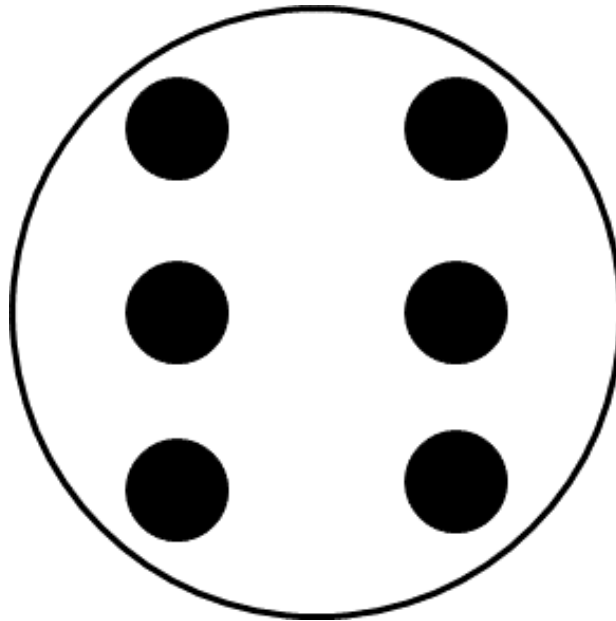
Figure 3.2 A six spot grid was used to characterize the microstructural uniformity within and between doped AlN samples. A series of SE and BSE SEM micrographs was taken at each spot. These micrographs were then compared for uniformity.

3.4 Measurement of hardness and fracture toughness via Vickers indentation

AlN and Tb:AlN samples to be tested by Vickers indentation were wet polished with successively finer grits of diamond abrasive wheels followed by alumina paste on felt wheels to 0.5 μm abrasive particle size. Vickers indentations were made on a Wilson Tukon 2100 using $F = 10$ Kgf indentation force. Under these indentation conditions, uniform easily measureable indents and cracks were produced. In addition we measured two commercially available materials, laser quality single crystal Nd:YAG (1.1 % Nd, Litton Industries) and undoped, polycrystalline AlN (Coorstek AlN 170). The indents used for hardness and fracture toughness measurements on Nd:YAG were made using $F = 0.25$ kgF indentation force since the YAG samples shatter using $F = 10$ kgF indentation force. An example of the indents produced from Vickers indentation of our Tb:AlN samples can be seen in **Figure 3.3**. A micrograph of an indent on Nd:YAG is included for comparison. The indent diagonals and crack lengths were measured using an optical microscope, and the Vickers hardness was then calculated using the relation:

$$HV = \frac{(F) \cdot 2 \sin(^{136°}/_2)}{d^2} \approx \frac{1.8544F}{d^2} \approx \frac{1.85F}{d^2} \qquad \text{Eq. 6}$$

where F is the applied load in Kgf and d is the average length of the diagonal in mm. The mode 1 fracture toughness, K_{IC} was calculated using the Niihara relation as described in [39], with data measured using the indentation procedure described above as follows:

$$K_{IC} = 0.035 a^{\frac{1}{2}} E^{\frac{2}{5}} H^{\frac{3}{5}} \left(\frac{l}{a}\right)^{\frac{-1}{2}} \phi^{\frac{-3}{5}} \qquad \text{Eq. 7}$$

where a is the half diagonal, E is the Young's modulus, H is the Vickers hardness, l is the crack length, ϕ is the constraint factor usually ≈ 3 and $E = 308$ GPa.
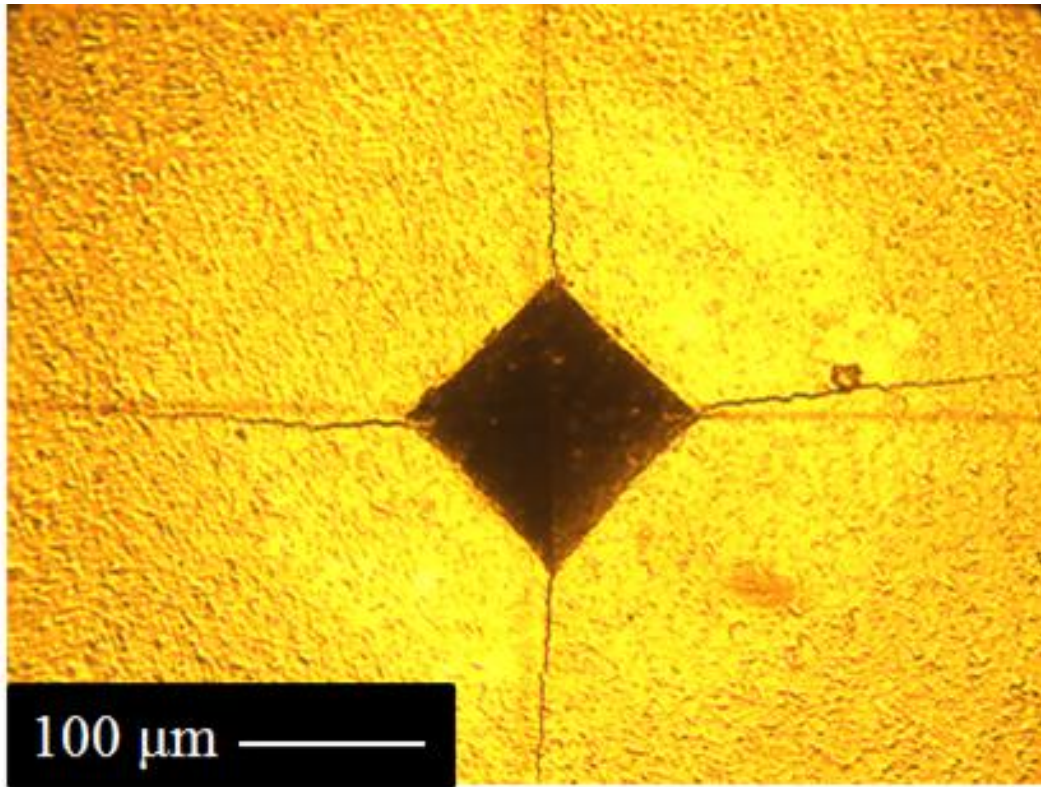
Figure 3.3 Optical micrograph of a typical vickers indentation in our AlN samples, clearly identifiable indents and cracks were produced which could be easily measured, allowing the calculation of mechanical properties including Vickers hardness (HV) and mode *I* fracture toughness (K$_{IC}$).

3.5 Thermal conductivity measurement

Thermal conductivity measurements were made in collaboration with C. Dames and Z. Wang. Due to the significant influence of thermal conductivity on the power limits of laser host materials (**Eq. 5**), it is important to understand the influence of microstructure (both grain size and grain boundary cleanliness) and dopant concentration on the thermal conductivity of RE doped AlN. A standard 3ω method [15] was used to measure the thermal conductivity of these samples. A narrow gold line was deposited on the well-polished surface of each sample using standard microfabrication techniques.

Each heater line was 10 µm wide, 250 nm thick (including a thin chromium adhesion layer), and patterned in a four-point probe configuration with 1 mm between the inner voltage probes. There was no need for a dielectric insulation layer between the heater line and substrate because AlN is already an electrical insulator, as further confirmed by probing with a multimeter on each sample. The thermal wavelengths used are at least 40 µm, ensuring that this measurement yields an effective average thermal conductivity over many grains. Measurements were conducted in a high vacuum cryostat over a temperature range from 80 K to 310 K (up to 475 K for two samples).

3.6 Calculation of thermal shock figure of merit

As mentioned previously, the tolerance of a material to thermal gradients can be described by the parameter R_s is given by **Eq. 5**. The fracture stress was not measured in this study; instead we used the measured indent K_{IC} values and the following equation in order to approximate the fracture stress:

$$\sigma_f = \frac{K_{IC}}{(\pi c)^{\frac{1}{2}}} \qquad\qquad \text{Eq. 7}$$

where c is the maximum flaw size. A highly conservative value of 20 µm was used for c. These approximate fracture stresses along with measured thermal conductivity, k (at 310 K) were used to calculate the thermal shock figure of merits using **Eq. 5**. In the calculation,

we used $\alpha = 2.7 \times 10^{-6}$ K^{-1}, $E = 308$ GPa and $v = 0.22$ [50]. The following values were used

for the comparison Nd:YAG sample $\alpha = 7.9 \times 10^{-6}$ K^{-1}, $E = 280$ GPa and $v = 0.25$ [20].

3.7 Characterization of crack morphology

The resulting cracks from Vickers indentation were imaged using SEM

microscopy and characterized as described schematically in **Figure 3.4**. This allowed

comparisons of the energy consumed by crack propagation to be made between samples

by comparing the average tortuosity of the cracks with the nominal crack length. In order

to quantitatively compare the geometry of the crack paths we examined sections of

indentation-induced cracks. For each sample, crack segments, lengths and deflection

angles were measured. The total crack path length is given by the sum of all crack

segments measured as:

$$l_{tot} = \sum_{i=1}^{n} l_i \qquad \text{Eq. 9}$$

where n is the number of segments. The average crack segment length is given by:

$$\bar{l} = \frac{\sum_{i=1}^{n} l_i}{n} \qquad \text{Eq. 10}$$

Similarly the average deflection angle is given by:

$$\bar{\theta} = \frac{\sum_{i=1}^{m} \theta_i}{m} \qquad\qquad\qquad \text{Eq. 11}$$

where m is the number of angles measured. Finally, the ratio of the total crack length to the crack path length of an un-deflected crack (l_{tot}/L) can be compared.
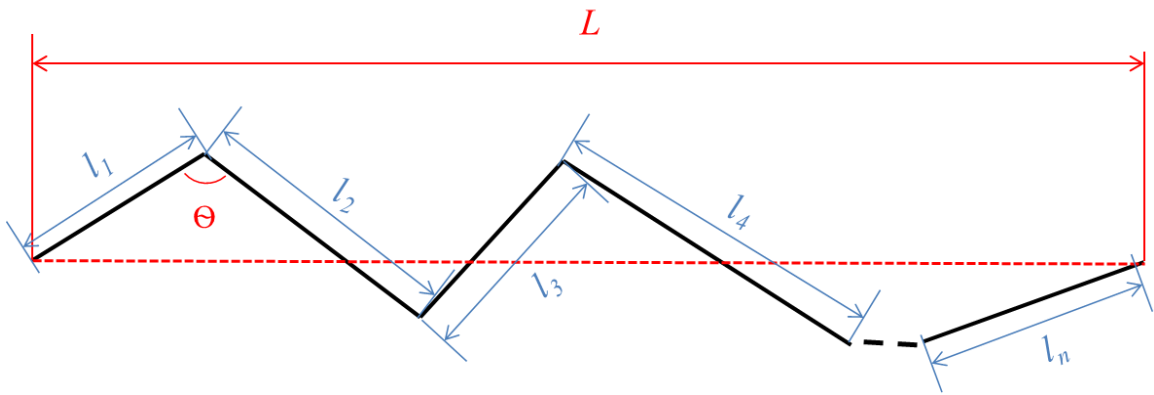
Figure 3.4 Schematic description of crack tortuosity and morphology characterization methodology. [54]

3.8 Annealing

In order to study the influence of annealing or post densification heat treatment on PL intensity, doped samples were cut in half and one half was placed in a tube furnace under flowing nitrogen at 700 °C for 8 hours. The PL measurements for both halves of the sample were then made on the same day under the same conditions.

3.9 Photoluminescence measurements

PL measurements in the visible range (Tb:AlN) were conducted using a Spex Fluorolog 3 spectrophotometer with a tungsten deuterium lamp with monochromators as a light source. Emission measurements were conducted using a 1 s integration time, 1 nm step size, and 3nm bandpass slits. PL measurements on Nd:AlN were conducted on an Horiba Jobin Yvon Fluorlog using an 808 nm laser diode as an excitation source. All PL measurements were done with the sample at room temperature.

4.0 Undoped and Tb doped AlN results

4.1 Undoped AlN

Initially the first main goal of this project was to see if the authors could produce highly translucent undoped AlN without the help of sintering additives which may hinder later attempts to dope for photoluminescence, while maintaining optical quality. **Figure 4.1** shows a plot of processing temperature vs relative density for undoped AlN samples processed with CAPAD, photographs taken over backlit text of samples processed at the three highest temperatures are also shown to illustrate the improvement in translucency with increasing relative density from increasing processing temperature. It can be seen that by 1600 °C Near full relative density was achieved without the use of sintering additives.

In parallel with the development of processing parameters, the influence of planetary ball milling on AlN samples densified with CAPAD was investigated. It was found that milling atmosphere, ball material and jar material significantly affect the final quality of the sample. **Figure 4.2** Shows a visual comparison of samples processed from

powder that was planetary ball milled under various conditions. All three samples were

photographed on a light table with the sample sitting on backlit writing. Sample (a) was

milled in air with stainless steel balls and transmits very little light. Sample (b) was also

milled with stainless steel balls but under an argon atmosphere. The third and lightest

colored sample (c) was milled under argon atmosphere with silicon nitride balls. As is

expected with optical materials, even small amounts of contamination significantly

influence the quality of the samples, and very easily cause degradation of the final

quality.
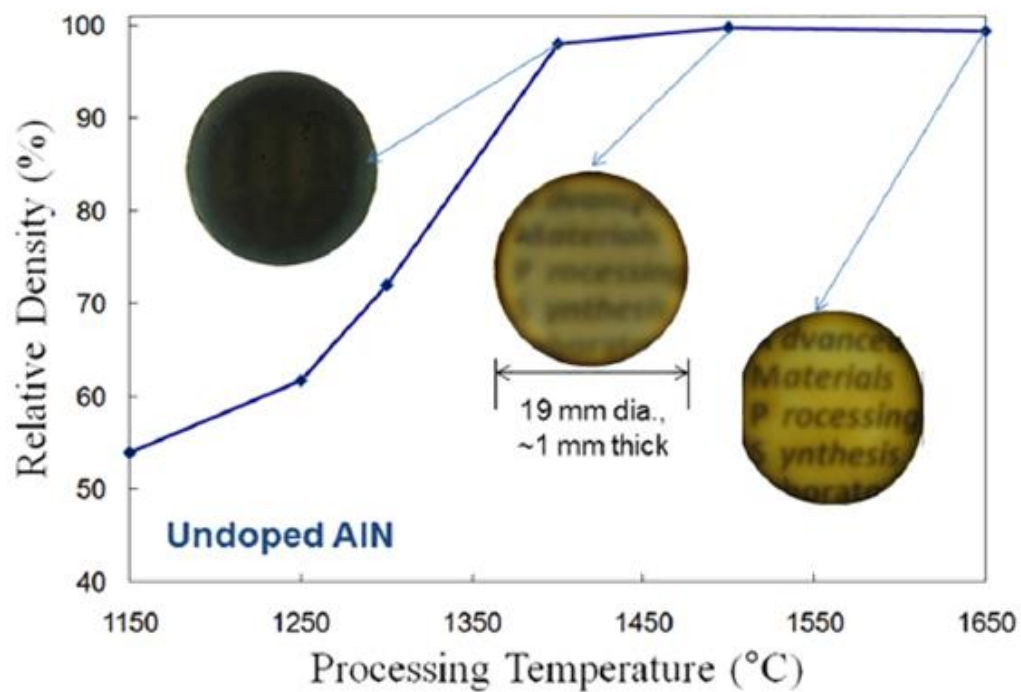
Figure 4.1 The effect of processing temperature on the relative density of CAPAD-processed pure AlN. The ceramics produced at temperatures greater than 1450 °C have relative density above 99%. The insets in the figure are photographs of the resulting samples processed at 1400, 1500, and 1650 °C, on top of backlit printed text. [53]
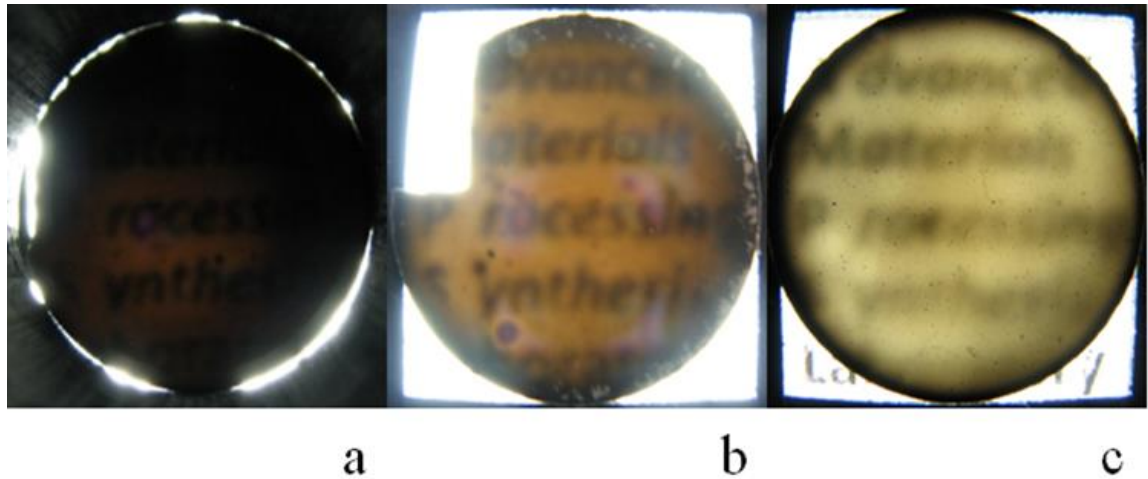
Figure 4.2 Influence of milling media and milling atmosphere on undoped AlN samples that were planetary ball milled prior to CAPAD processing. (a) stainless steel balls in air (b) stainless steel balls in argon (c) silicon nitride balls in argon. Samples are sitting on top of backlit text.

4.2 Tb doped AlN for visible PL emission

Having established powder and CAPAD processing parameters for producing highly translucent undoped AlN without the use of sintering additives, we turned to the goal of doping bulk polycrystalline AlN for visible PL emission with Tb. The solubility of RE ions in the AlN lattice is low because of the mismatch in ionic radii between REs and Al. Rare earth oxides are often used as sintering aids for hard to sinter ceramics including AlN and have been previously used as a RE source when attempting to dope AlN with RE.[20] However, using oxides as a RE source for doping poses several problems. First, doping Tb onto Al sites from a Tb oxide source is a two-step process involving the dissociation of a stable oxide followed by diffusion of the Tb into the aluminum nitride lattice. Second, it is well known that oxygen contamination reduces the thermal conductivity of AlN,[48,21,22] a serious problem for high-power optical applications (the defect behavior associated with oxygen contamination in aluminum

27

nitride has been described by [27] as oxygen substitution onto a nitrogen site with O_N/V_{Al} = 3 at low concentrations and defect clusters at higher concentrations). For these reasons, we chose to use pure Tb and TbN as Tb dopant sources. Doping with pure Tb requires no disassociation of a stable oxide, but the placement of Tb on Al sites still leaves excess Al, which again is expected to reduce thermal conductivity and also adversely affect optical properties. This problem is removed by using TbN as a dopant source, since TbN and AlN have the same stoichiometric quantity of N.

We also conjectured that high energy ball milling (HEBM) would help with the doping process and produce a better final result. There is ample evidence that HEBM is effective for mixing, grain size refinement, and mechanical alloying. Previous work has also shown that it can increase the solid solubility.[23] To test the effectiveness of doping via ball milling, we experimented with both Tb and TbN source powder using low energy ball milling (LEBM) or HEBM prior to CAPAD processing. Two different Tb doping concentrations were used, 0.25 at. % and 0.5 at. % Tb. **Figure 4.3** shows xrd data for both doped and un-doped AlN processed under various conditions and within the resolution of x-ray diffraction, all peaks can be attributed to AlN.
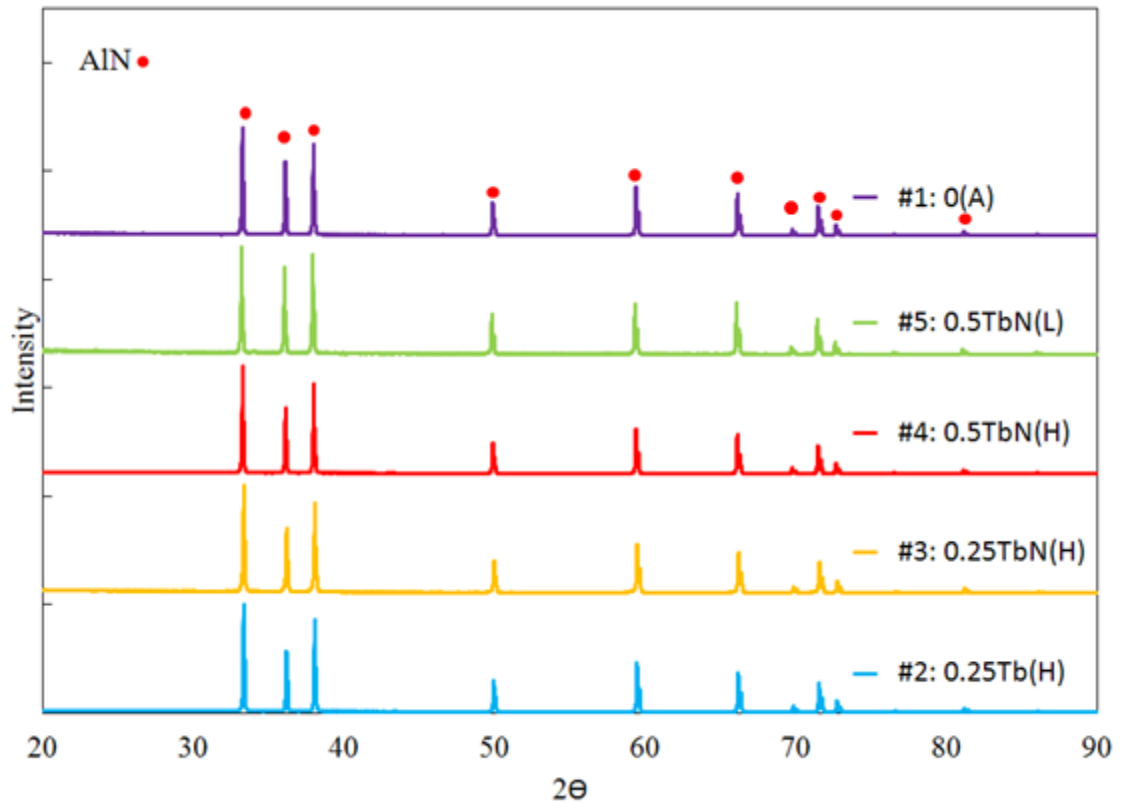
Figure 4.3 X-ray diffraction data for Tb doped and undoped aluminum nitride samples compared in this study. All of the peaks correspond to hexagonal AlN and are marked with a red dot. [54]

The effect of doping with Tb versus TbN can be appreciated by comparing

Figures 4.4(a) and **4.4(b)**. **Figure 4.4(a)** shows secondary electron (SE) and back

scattered electron (BSE) micrographs of AlN doped with 0.25 at. % Tb. **Figure 4.4(b)**

shows the result of the identical concentration of Tb (0.25 at. %) but using TbN as the

dopant source. Although the Tb concentration is the same in both cases, the Tb-source

sample (**Figure 4.4(a)**) shows more segregation at the grain boundaries. In the TbN case

(**Figure 4.4(b)**), Tb segregation is limited to triple points. Since TbN is a better source

material, we used nitrided RE powder for the remainder of the experiments in this work.

The effect of HEBM milling in doping AlN with Tb in combination with the influence of dopant source selection are presented in **Fig 4.5** The influence of dopant source alone can be seen in **Figure 4.5(a,b,c,d)** shows SE and BSE micrographs for 0.25Tb:AlN with Tb and TbN as the dopant source respectively. **Figure 4.5(e,f,h,i)** shows two samples that were prepared with the same concentration of 0.5 at. %Tb with TbN as dopant source using identical CAPAD conditions, but the reactants for the sample in **Figure 4.5(h,i)** were mixed using LEBM while the sample in **Figure 4.5(e,f)** was produced using HEBM. The micrographs clearly reveal significantly less segregation at grain boundaries in **Figure. 4.5(f)**, indicating that the Tb dopant is likely more homogeneously distributed in the HEBM case. Further evidence that this is the case is given below. The effectiveness of HEBM is likely due to the simultaneous break up of AlN particles and mechanical alloying with TbN. While it is clear from **Figure. 4.5(f)** that little segregation is observed with the combined strategies of using TbN source material and HEBM, it is still not clear that the Tb was incorporated in the AlN grains.
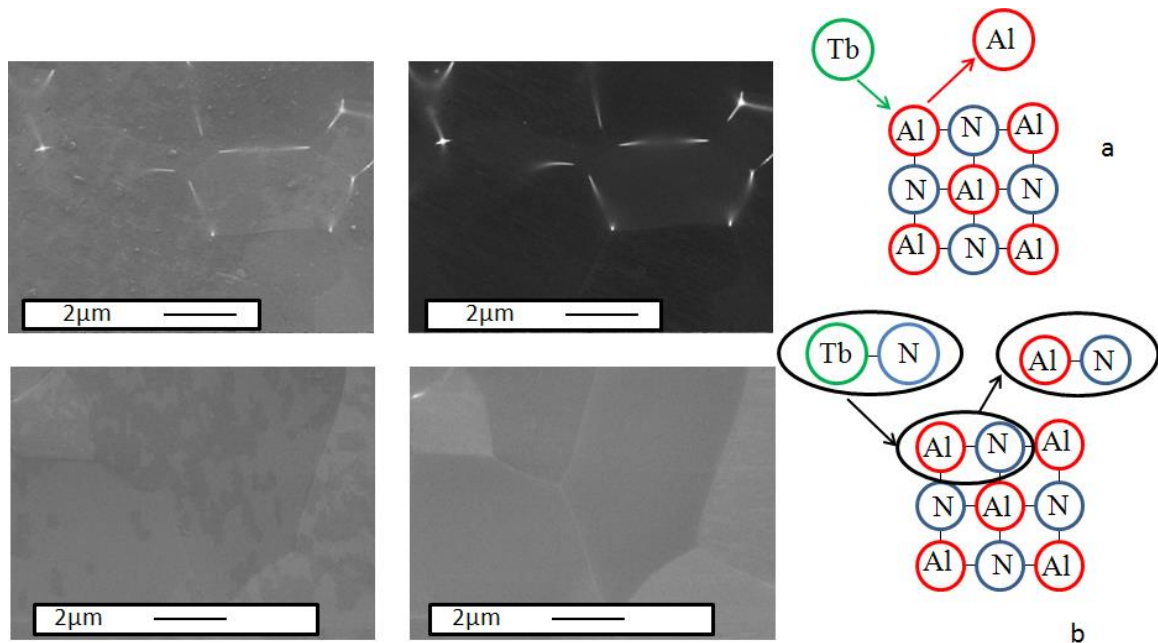
Figure 4.4 Microstructural evidence for the advantages available from careful dopant source selection and a schematic description of why. (a) Tb dopant source (b) TbN dopant source. Both samples doped with 0.25 at% Tb. Use of TbN as a dopant source allows stoichiometry to be maintained.

To assess if there is Tb present in the AlN grains, we performed STEM on a 0.5 at. % Tb:AlN sample produced with TbN and HEBM. **Figure 4.6** is a bright field STEM image of the Tb:AlN ceramic showing multiple grains separated by grain boundaries, along with EDS elemental maps of Al, N, and Tb. The image was captured so that the sample covers most of the image except for a small region in the upper right hand corner, which ensures that colors in elemental maps can be distinguished from background signals. The Al and N maps reveal that as expected, these two elements are present throughout the sample (note that where there is no sample the elemental maps are completely black). The Tb map clearly shows that although there is some Tb segregation

at grain boundaries, Tb is also clearly present in the grain interiors, confirming that Tb

has been doped into the AlN matrix.

a) Scale ——— 2μm SE	c) Scale ——— 2μm SE	e) Scale ——— 2μm SE	h) Scale ——— 2μm SE
b) Scale ——— 2μm BSE	d) Scale ——— 2μm BSE	f) Scale ——— 2μm BSE	i) Scale ——— 2μm BSE
Sample 2	Sample 3	Sample 4	Sample 5
0.25 Tb HE	0.25 TbN HE	0.5 TbN HE	0.5 TbN LE
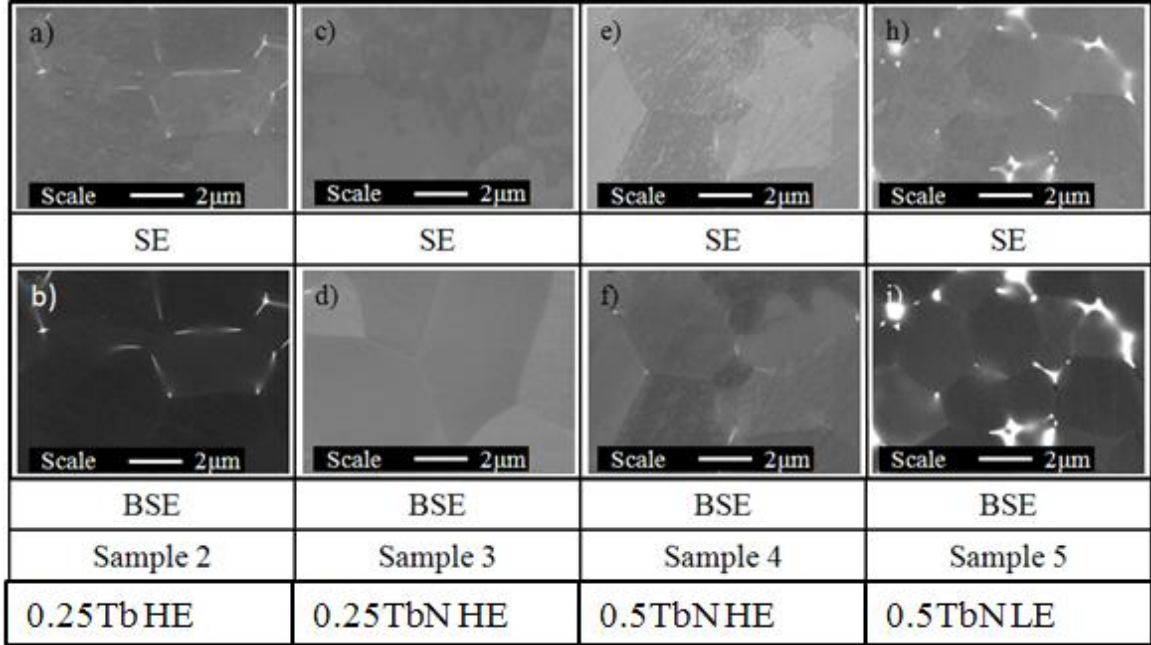
Figure 4.5 SEM micrographs of Tb:AlN samples demonstrating the effects of dopant
source [(a,b) and (c,d)] and milling method [(e,f) and (h,i)]. For example, (a,b-c,d) shows
SE and back scattered electron (BSE) micrographs of AlN doped with 0.25 at. % Tb,
using Tb as the source for (a,b) and TbN as a source for (c,d). both prepared prepared
using high energy planetary ball milling. To examine the influence of milling energy (e,f)
and (h,i) used the same dopant percentage and source while changing the milling energy.
The difference in segregation is significant.[54]

Figure 4.7(a) is a photograph of a Tb:AlN ceramic doped with 0.5 at. % Tb on top of

backlit text, demonstrating translucency. In addition to transmitting light, the Tb:AlN

displays photoluminescence. **Figure 4.7(b)** compares the room temperature PL

measurements of an un-doped AlN sample and the 0.5 at. % Tb:AlN sample when

excited with a 300 nm light source. The un-doped sample shows a very broad peak from

about 350 nm to 550 nm, with a maximum at 420 nm. Similar broad peaks have been

observed in nominally un-doped AlN before [24,25] and are usually attributed to oxygen

impurity defects or nitrogen vacancies. We believe that the broad peak observed here is likely due to similar point defects. By contrast, the Tb:AlN PL spectrum shown in **Figure 4.7(b)** displays two much sharper peaks that are characteristic of Tb transitions $^5D_4\rightarrow^7F_6$ centered at 491 nm and $^5D_4\rightarrow^7F_5$ centered at 550 nm. These transitions are labeled according to the Dieke diagram.[26] It is worth emphasizing that **Figures 4.7(a)** and **4.7(b)** confirm that the Tb:AlN ceramic transmits and emits visible light, both prerequisites necessary for a good host material. **Figure 4.7(c)** shows an excitation spectra for Tb:AlN monitoring at 491 nm and scanning the excitation wavelength from 265-415 nm. It was observed that by heating the sample post processing in a tube furnace under nitrogen atmosphere, the PL intensity could be improved. **Figure 4.8** shows PL under 300 nm excitation from two halves of the same sample that was cut in half after polishing. The half that was heated shows more intense PL emission than the as processed half.
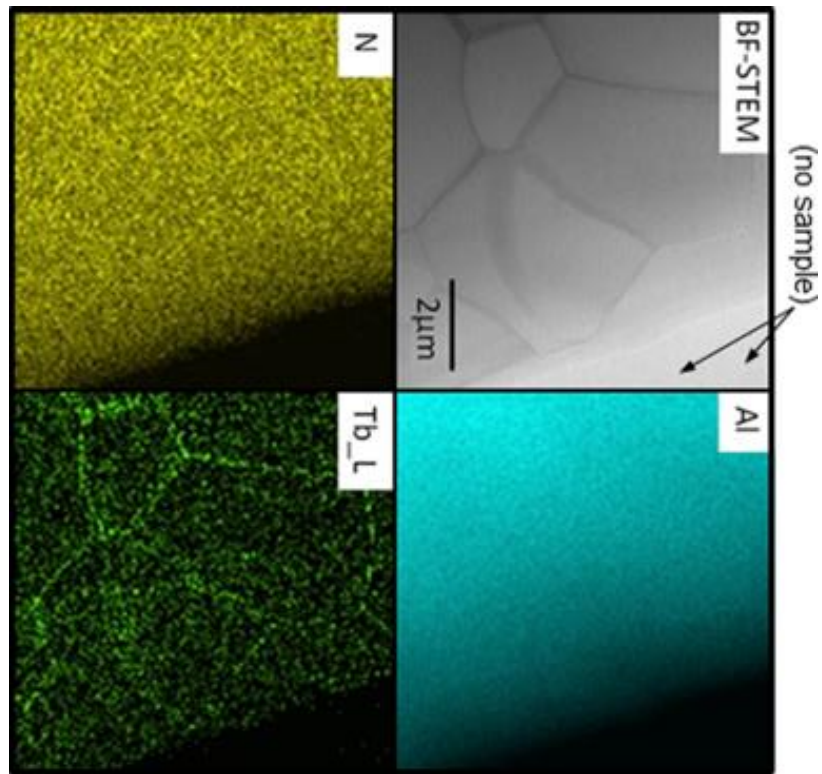
Figure 4.6 Bright field STEM image of the 0.5at. %Tb:AlN bulk ceramic showing multiple grains separated by grain boundaries, along with EDS elemental maps of Al, N, and Tb (L-line). There is no sample in the upper right hand region hence the elemental maps are completely black. The Tb elemental map reveals Tb in the grain boundaries as well as the grain interiors confirming doping. [53]
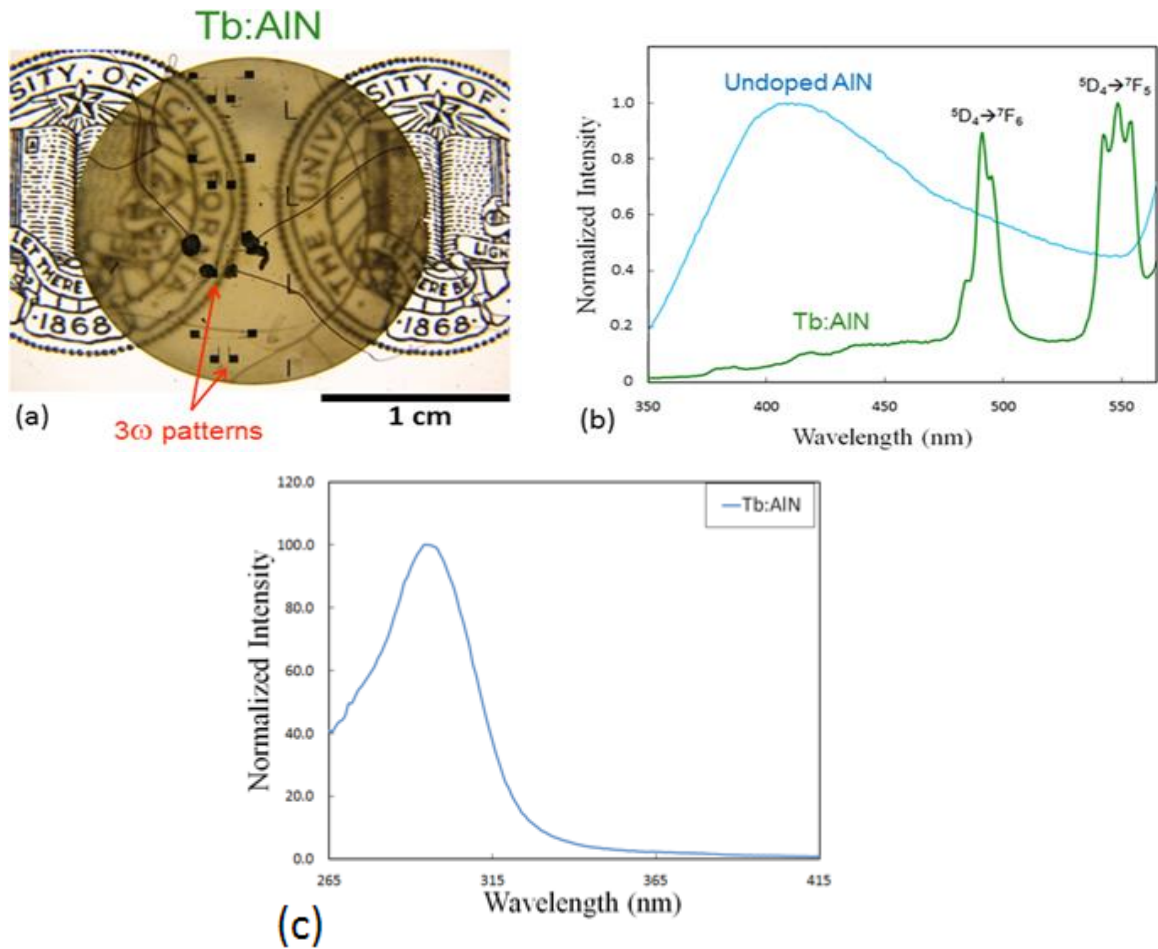
Figure 4.7 Photograph and PL measurements of the 0.5 at. %Tb:AlN ceramic. (a) A photograph of the sample on top of backlit text, demonstrating translucency. (b) Comparison of the PL measurements of an undoped AlN sample and the 0.5 at. % Tb:AlN sample when excited with a 300 nm light source. The undoped sample shows a very broad peak from about 350 nm to 550nm, with a maximum at 420 nm. The Tb:AlN PL displays two much sharper peaks that are characteristic of Tb transitions $^5D_4 \rightarrow {}^7F_6$ centered at 491 nm and $^5D_4 \rightarrow {}^7F_5$ centered at 550 nm. (c) Shows excitation spectra for Tb:AlN monitoring at 491 nm and scanning the excitation wavelength from 265-415 nm. [53]
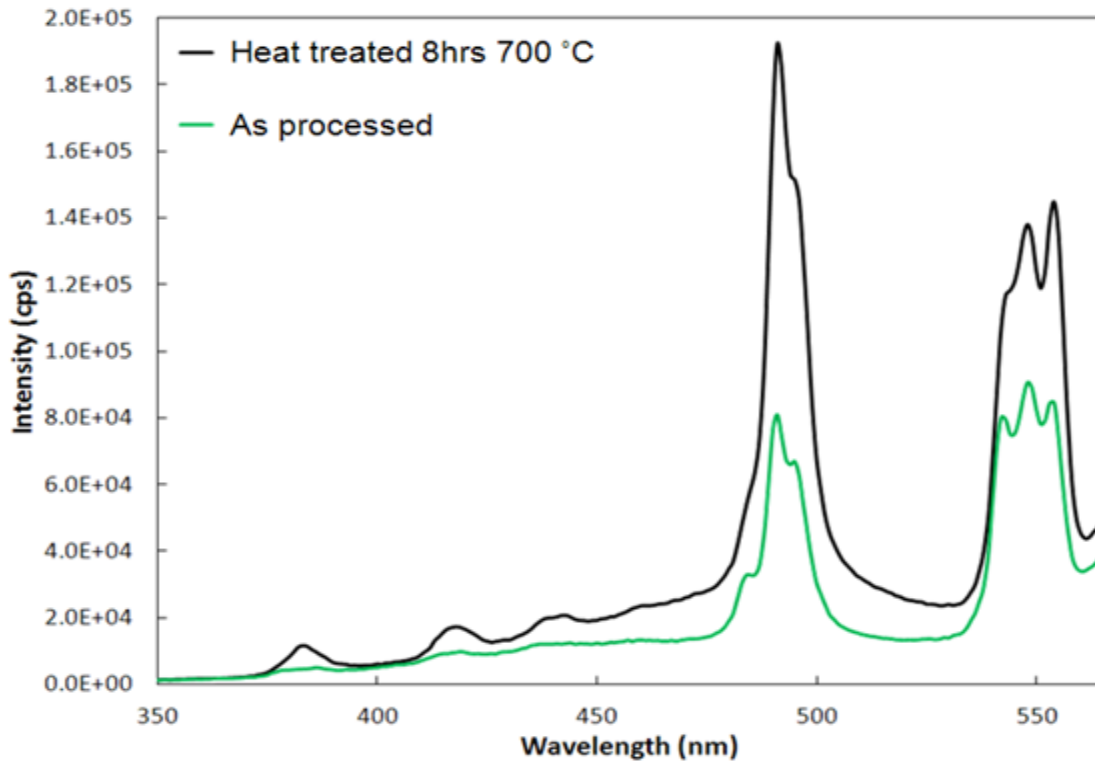
Figure 4.8 PL measurements showing the effect of heat treating on PL intensity in Tb:AlN. Heat treating the sample provides nearly 2.5 times better PL intensity from the Tb peak at 491 nm as shown by the black trace (post annealing) as compared with the green trace. Measurements and heat treating were conducted as described in sections **3.8** and **3.9.**

4.3 Mechanical properties of Tb doped AlN

Table 3 lists the samples tested, dopants and concentrations, and a summary of the properties observed for AlN and Tb:AlN samples. The results reveal that despite significant differences in grain size and dopant segregation, the hardness and indent fracture toughness values are actually quite similar. As discussed in detail below, we believe that grain boundaries and segregation do not significantly alter the crack propagation or plastic flow of the samples, implying that grain boundaries have similar mechanical properties whether or not they have significant dopant segregation.

Sample	Processing parameters Mol% dopant source(Ball milling energy)	Grain size (μm)	Vickers hardness, HV $(\frac{Kgf}{mm^2})$	K_{1c} $(MPam^{\frac{1}{2}})$	Thermal conductivity, k @ 310K $(\frac{W}{m \cdot K})$	Thermal shock parameter, R_s $(\frac{W}{m})$
1	none	2.6	1154	5.0	60	36000
2	0.25Tb(H)	4.2	1136	4.4	77	36000
3	0.25TbN(H)	4.7	1045	4.8	91	52000
4	0.5TbN(H)	4.3	1150	4.4	94	48000
5	0.5TbN(L)	3.3	1180	4.2	75	38000

Table 3 Summary of doping and processing parameters along with measured and calculated mechanical and thermo-mechanical properties for Tb doped AlN samples presented. [54]

Figure 4.10 shows Vickers hardness (*H*v) plotted vs. grain size. The hardness values range from 1045 to 1180 kgF/mm^2. Overall there is a ~12% difference in hardness between the sample with the highest hardness (Sample 5) and the lowest (Sample 3). It should be noted that the hardness does not follow a Hall–Petch (d$^{-1/2}$) trend. Four of the Samples (1, 2, 4 and 5) have virtually identical hardness (only 3% difference) despite nearly a doubling in grain size. The degree of dopant segregation also does not play a significant role. For example samples 4 and 5 have drastically different dopant segregation (see **Figure 4.5**), yet the change in hardness is only minimal. Thus there is only a minimal effect of grain size and/or dopant segregation on hardness. The commercial single crystal Nd:YAG and polycrystalline commercial AlN we measured for comparison had a hardness of 1745 and 1152 kgF/mm^2. The results show that our samples are similar to the commercial.

An example of the indents produced from Vickers indentation of our Tb:AlN samples can be seen in **Figure 4.9**. An optical micrograph of an indent on Nd:YAG is included for comparison. The indents used for hardness and fracture toughness measurements on Nd:YAG were made using F = 0.25 kgF indentation force since they shatter using a F = 10 kgF indentation force. **Figure 4.9 b** gives an example of the indents produced in AlN under F = 0.25 kgF indentation force used to test YAG samples.
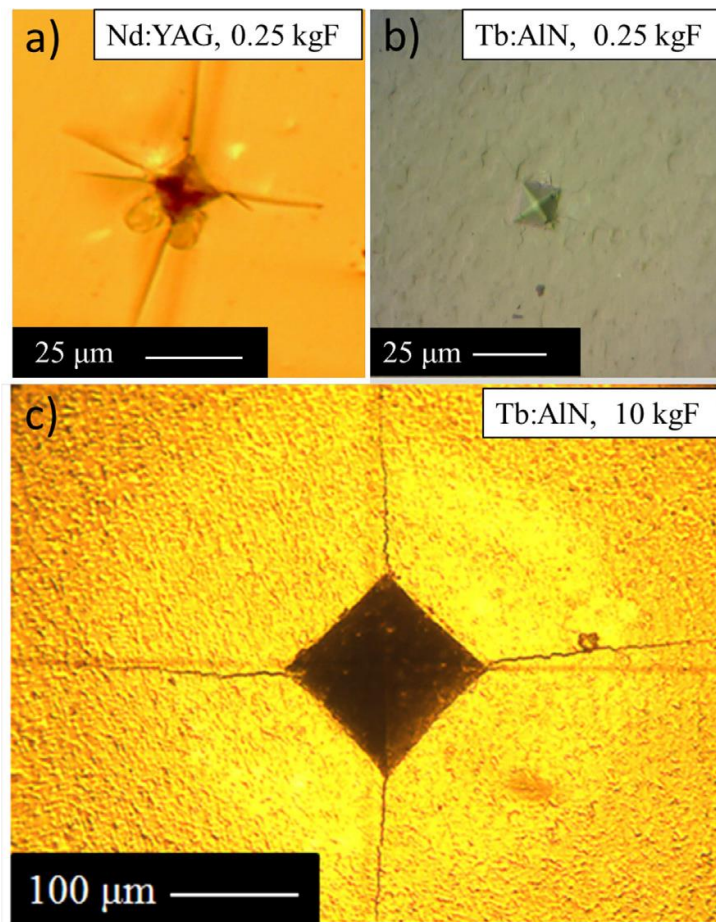
Figure 4.9 Examples of indents and the corresponding cracks that resulted from Vickers indentation in the various samples reported here. The crosshairs from the filar eyepiece on the microscope are also visible in some cases. (a) Single-crystal Nd:YAG with indentation force F = 0.25 kgF, showing distinct cracks. (b) Tb:AlN with indentation force F = 0.25 kgF, showing very minor cracks. (c) Tb:AlN with indentation force F = 10 kgF.
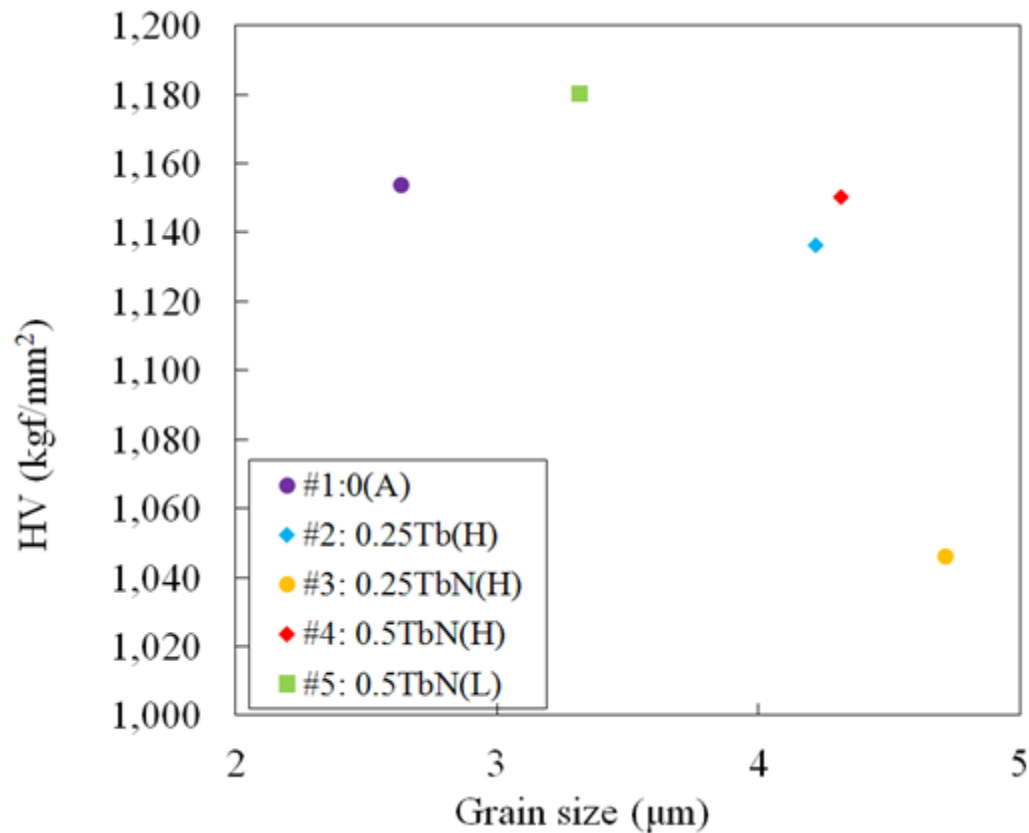
Figure 4.10 Vickers hardness values for doped and undoped samples with respect to grain size. The calculated vickers hardness changes very little with changing grain size in this region. [54]

Figure 4.11 shows indent fracture toughness, K_{IC} vs. grain size. Similar to hardness, the changes are not large, and there is only a 16% change for K_{IC}. The undoped (Sample 1) has the smallest grain size and the highest fracture toughness. The doped samples appear to have an opposite trend, i.e. the K_{IC} increases with increasing grain size. However as mentioned previously, the changes are minor. The commercial Nd:YAG we measured for comparison had an indent fracture toughness of 1.35 MPa.m$^{0.5}$. This value is similar to previously reported indent fracture toughness measurement on YAG single crystals of 1.48 MPa.m$^{0.5}$ [20]. The measured value for commercial AlN was 4.45 MPa.m$^{0.5}$, which falls in

the range of our samples indicating that AlN and Tb:AlN measured on our samples is similar to high quality commercial AlN.
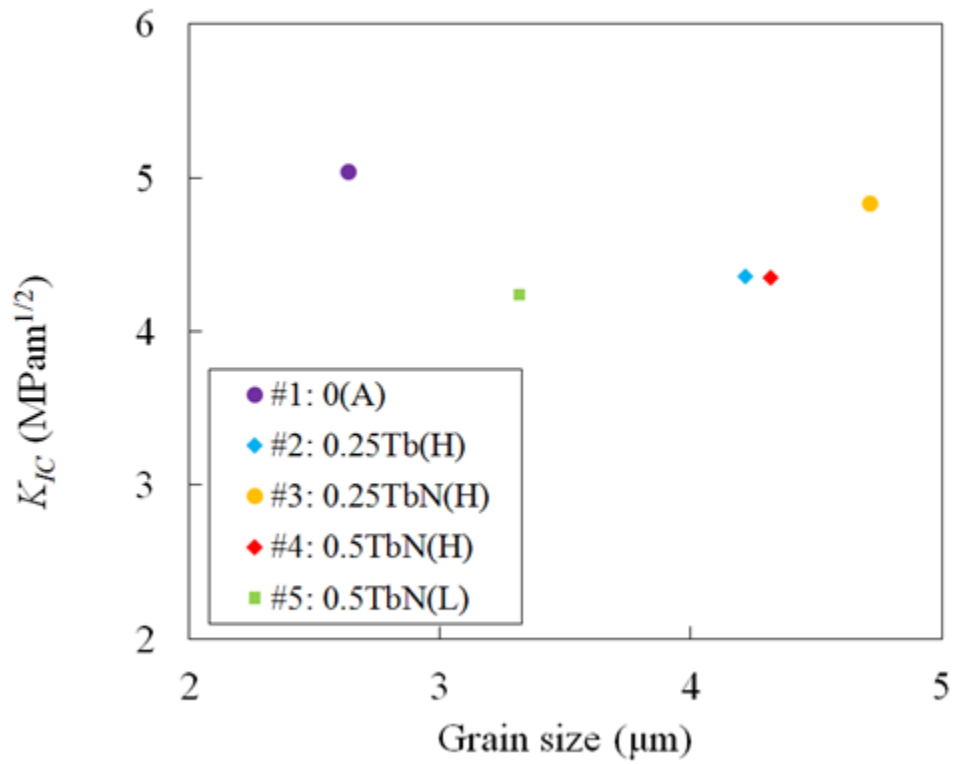
Figure 4.11 Indent fracture toughness values vs. grain size for AlN and Tb:AlN samples. [54]

	a	b	c
	SE	SE	SE
	BSE	BSE	BSE
	Sample 1	Sample 4	Sample 5
	Undoped	0.5At% Tb as TbN	0.5At% Tb as TbN
	Unmilled	High energy planetary mill	Low energy ball mill
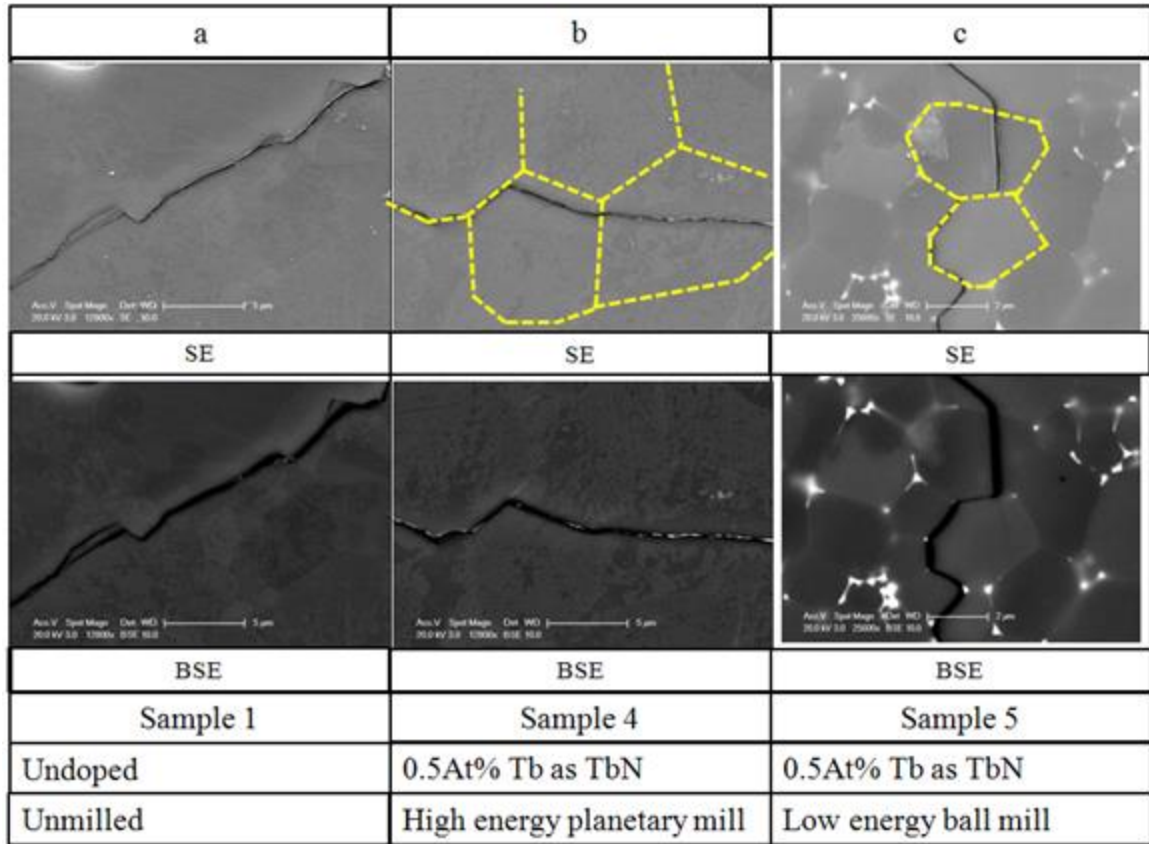
Figure 4.12 SEM micrographs of cracks resulting from microindentation in samples with very different amounts of dopant segregation (sample 4, a and b) and sample 5 (c and d). Grain boundaries have been highlighted in yellow to help better visualize the mixed inter/intra-granular crack path. [54]

Sample	Average deflection angle, $\bar{\theta}$ (Degrees)	Average segment length, $\bar{l}$ (µm)	l_{tot}/L
1	119.5	3.42	1.119
4	123.9	3.96	1.094
5	118.0	2.52	1.112

Table 4 Summary of crack tortuosity characterization results in Td:AlN. Crack tortuosity was characterized according to the procedure described in section **3.7.** [54]

We believe the similar toughnesses observed in all samples despite the large difference in grain sizes and grain boundary segregation is due to similar crack propagation behavior across samples. Evidence of similar crack patterns is provided in **Figure 4.12** showing both SE and BSE scanning electron micrographs of un-doped AlN **Figure 4.12a** and doped AlN **Figures b** and **c**). In both doped and un-doped samples, we observe inter-granular as well as intra-granular fracture, *i.e.* it can be seen that the crack passes through several grains and also follows grain boundaries in some places. This can clearly be observed in all three samples, however, because of the slight dopant segregation in (b and more so in c) the grain boundaries are more evident. Selected grain boundaries were outlined in yellow to make them more visible.

Crack propagation is related to the work needed to create new free surfaces. If a crack is propagating through a completely isotropic medium the crack would propagate as a straight line since there are no microstructural features to divert it. AlN has a hexagonal structure that could lead to crack deflection in a randomly oriented ceramic, since fracture energies are expected to be different along different crystallographic directions. The anisotropic nature of crack propagation could be compounded by anisotropic residual stresses in hexagonal AlN. In addition, dopant segregation at grain boundaries could divert the crack.

Crack diversion usually increase fracture toughness, since there is an overall larger surface area created. In other words, the higher the ratio of surface area created by a tortuous crack to a straight crack (A_{tor}/A_o), the higher the fracture toughness. If we assume that the crack widths, w (the penetration depth perpendicular to crack propagation

direction) are the same for the various samples, then a measure of crack tortuosity can be given by the ratio of the total crack path length, l_{tot} to the crack path length of an un-deflected crack (nominal crack length), L. **Figure 3.4** is a schematic showing the relationships between the deflection angles, θ, the crack path segments, l, the total crack path length, l_{tot} and the nominal crack length, L. The area ratio and length ratios can be related to path lengths and average deflection angle, $\bar{\theta}$ as follows:

$$\frac{A_{tor}}{A_o} = \frac{wl_{tot}}{wL} = \frac{l_{tot}}{l_{tot}\sin{\bar{\theta}}/2} = \frac{1}{\sin{\bar{\theta}}/2} \qquad \text{Eq. 12}$$

In order to quantitatively compare the geometry of the crack paths we examined sections of indentation-induced cracks as described in section **3.7**. We chose the samples with large differences in dopant segregation for examination. For each sample, crack segments, lengths and deflection angles were measured. The total crack path length is given by the sum of all crack segments measured as (from **3.7**):

$$l_{tot} = \sum_{i=1}^{n} l_i \qquad \text{Eq. 9}$$

where n is the number of segments. The average crack segment length is given by:

$$\bar{l} = \frac{\sum_{i=1}^{n} l_i}{n} \qquad \text{Eq. 10}$$

Similarly the average deflection angle is given by:

$$\bar{\theta} = \frac{\sum_{i=1}^{m} \theta_i}{m} \qquad \text{Eq. 11}$$

where m is the number of angles measured. Finally, the ratio of the total crack length to the crack path length of an un-deflected crack (l_{tot}/L) can be compared. These results are summarized in **Table 4**.

The average path segment length $\bar{l}$ varies between the samples from 2.5 to 3.4 μm. However, despite the large differences in dopant segregation, the average path length to crack length ratios (l_{tot}/L) are very similar for the three types of samples. Moreover, the average deflection angles measured are almost identical and very near 120°. These measurements confirm that the crack tortuosity is very similar in all three samples, indicating that dopant segregation at grain boundaries in Tb:AlN does not affect crack propagation behavior. It is interesting to note that using $\bar{\theta} = 120°$ in Eq.12 one gets 1.15 which is remarkably close to the measured (l_{tot}/L) which range from 1.09 to 1.12. These measurements confirm that the crack propagation is very similar in all three samples.

As mentioned above, toughness is expected to be related to crack tortuosity and since the (l_{tot}/L) ratio is a measure of crack tortuosity, it is not surprising that the samples have similar fracture toughnesses. Thus we conclude that despite notable differences in dopant segregation, the samples have similar fracture toughness because cracks have similar tortuosity.

4.4 Thermal conductivity of Tb doped AlN

The thermal conductivities of the samples reported here were measured as described in section 3.5. **Figure 4.13** gives a comparison of the thermal conductivity observed in this work with the thermal conductivity reported for Nd:YAG. A simulation of the temperature gradient in a laser rod for each of the thermal conductivities is also shown. The measured thermal conductivities k of all five samples are given in **Figure 4.14**. The data transition from increasing to decreasing $k(T)$ trends, with the peaks occurring in the range from 160 to 250 K. The thermal conductivity results reveal a much stronger dependence on sample microstructures than the mechanical properties – there is a 56% difference between samples at 310 K and an almost 100% change at peak. As discussed below, the data can be explained by considering grain boundary scattering as well as segregation at grain boundaries. These measurements are all much lower than what is expected for pure, single-crystal AlN, which, according to Slack et al. [4], decreases monotonically from around 9000 W m^{-1} K^{-1} at 80 K to 135 W m^{-1} K^{-1} at 500 K (assuming a 5.4 mm sample diameter). The basic trends of **Figure 4.14** are consistent with strong thermal conductivity reduction by grain boundary scattering of phonons, which in the low-temperature limit usually corresponds to $k(T)$ power laws ranging from T^2 to T^3 [17], becoming constant at high T. The importance of grain boundary scattering in these samples is reinforced by **Figure 4.15**, which shows that the thermal conductivity generally increases with the average grain size, although there is also substantial scatter among the different samples. In addition, the decreasing $k(T)$ trend at higher T is a well-known signature of Umklapp scattering, and impurity scattering may also play a role near the peak. It is

noteworthy that the observed reductions in thermal conductivity in **Figures**. **4.14** and **4.15** are much stronger than those predicted by Slack et al. [4] for a 1 µm grain boundary scattering length and allowing for oxygen impurities (4.2 x 10^{19} cm^3 , or 0.04 at.%). Those calculations found the micron-grained sample to be virtually indistinguishable from the equivalent bulk sample above 200 K (at which point k = 540 W m^{-1} K^{-1}), with both decreasing to around 125 W m^{-1} K^{-1} at 500 K. At lower temperatures the calculation for the 1 µm polycrystal diverges from the bulk sample, with the former exhibiting a peak of around 730 W m^{-1} K^{-1} at 120 K. Thus, simple grain boundary scattering as considered in Ref. [4] cannot explain our measurements, since the present samples have larger grains (2–5 µm, as compared to 1 µm) yet much lower thermal conductivities, by factors ranging from 2 to more than 10. Our samples may also be expected to experience stronger impurity scattering than considered in Ref. [4] due to the larger dopant concentrations (0.25–0.5 at.% Tb), but no amount of impurity (Rayleigh) scattering can explain the limiting trends of **Figure 4.14** at both low and high T. Instead, to understand these measurements, it is essential to recognize that dopant segregation at the grain boundaries dramatically increases the strength of grain boundary scattering for a fixed grain size. A similar effect has been reported by Watari et al. [49]. For example, samples 2 and 3 have similar grain sizes and the same nominal dopant concentration of 0.25 at.% Tb. However, the micrographs in **Figure 4.5** show that sample 2 has more dopant segregation at the grain boundaries, and thus is expected to have lower thermal conductivity, consistent with the measurements in **Figure 4.14**. Overall, the thermal conductivity of these samples is best understood as being in a mixed regime, with strong grain boundary scattering (as modified

by dopant segregation) at all temperatures and Umklapp scattering also being important at

higher temperatures.
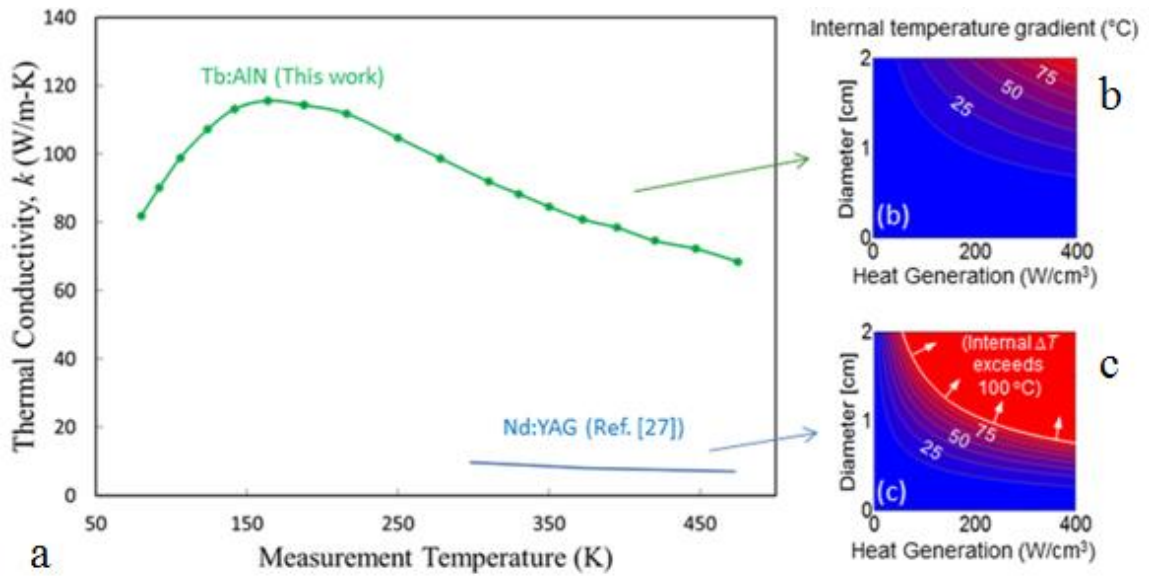
Figure 4.13 (a) Thermal conductivity, k, measurements of the 0.5 at. % Tb:AlN ceramic shown in Figs. 2(d), 3, and 4. Also plotted is the k of state of the art Nd:YAG. (b) and (c) are simulations comparing the internal temperature gradients within a rod of our Tb:AlN (k¼94 W/(m K)) and Nd:YAG (k¼14 W/(m K)), as functions of the rod diameter and volumetric heat generation rate. The higher k of Tb:AlN results in much smaller temperature nonuniformities than the state of the art Nd:YAG gain material. (Nd:YAG Redrawn from J. Li, Y. Wu, Y. Pan, W. Liu, L. Huang, and J. Guo, Opt. Mater. 31, 6 (2008). Copyright Elsevier Publishing.) [53]
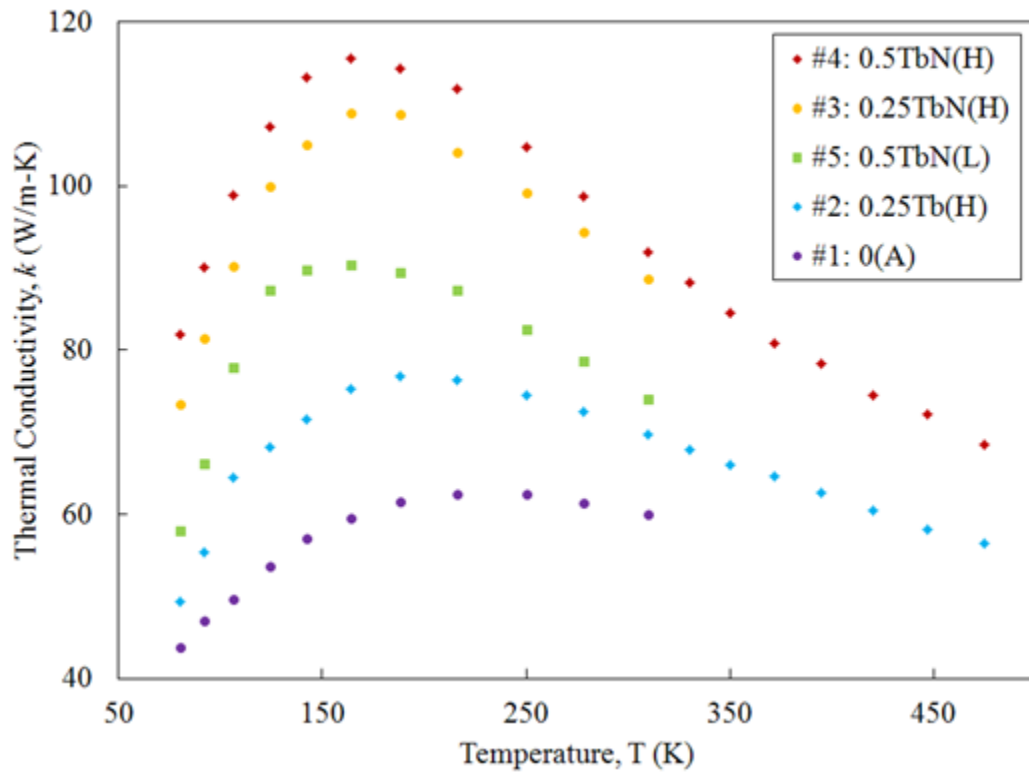
Figure 4.14 Measured thermal conductivities for undoped and Tb doped AlN. Thermal conductivity was measured using a standard 3ω as described in section **3.5**. [54]
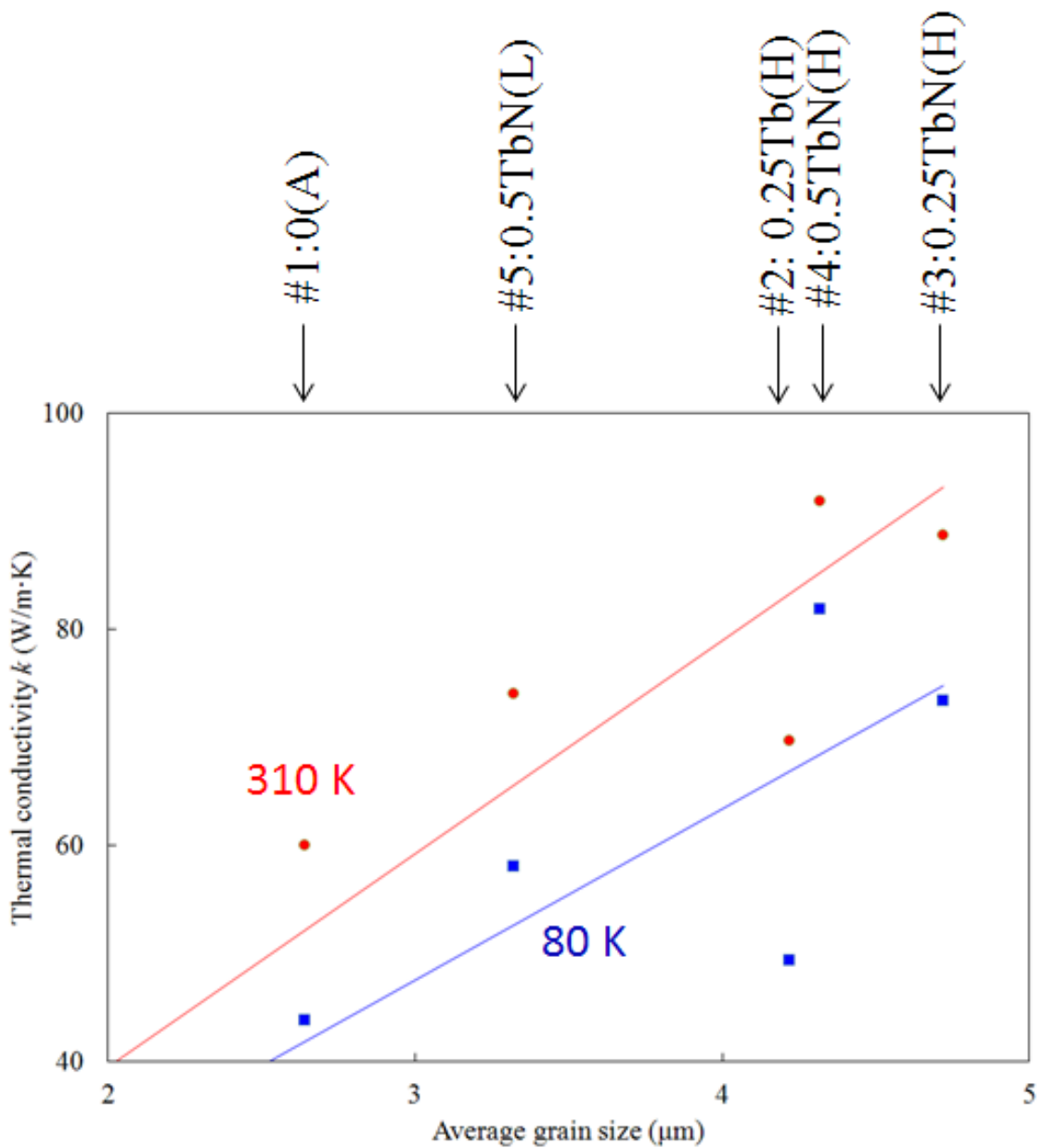
Figure 4.15 Measured thermal conductivity as a function of grain size, for two selected temperatures. Lines are straight-line fits passing through the origin, which is the limiting behavior expected if grain-boundary scattering dominates. [54]

4.5 Thermal shock resistance in Tb:AlN

Thermal shock is an important cause of failure in ceramics since they are typically used in high temperature applications. Thus the causes of thermal shock as well as methods to evaluate thermal shock performance have been well studied [21,22]. One common test condition is based on quenching samples from elevated temperature in water or oil. Alternatively, the samples can be cooled by impinging a fluid jet onto a sample at elevated temperature. These tests rely on the accurate measurement of a thermal gradient and thus are reliable for large samples. The optical quality ceramics produced in this study are considerably smaller than those typically used for structural applications, making accurate measurement of thermal gradients significantly more challenging. Considering the challenges, we use the thermal shock figure of merit R_s described in **Eq. 5**) to compare our samples.

This figure of merit can be thought of as describing the ability of a material to tolerate thermal loading while maintaining a thermal gradient smaller than that required to induce fracture. This parameter has been plotted against grain size in **Figure 4.16** for each sample tested. Since the fracture toughnesses, K_{IC} are relatively constant across the samples examined in this study but thermal conductivity varies significantly, we find that the changes in R_s are dominated by the thermal conductivity and show a strong grain size dependence.

In addition this figure of merit allows us to compare the thermal loading tolerance of different laser host materials, including Nd:YAG which has been reported to have an R_s value of 790 W/m [40]. The figure of merit, R_s calculated in this work using the same

procedure as Tb:AlN for Nd:YAG is 812 W/m, which is very close to previously report value. **Figure 4.17** compares the R_s value obtained in this work with well-known laser host material Nd:YAG. In contrast, the highest calculated Rs from the measurements conducted on Tb:AlN was 52,000 W/m. This high tolerance to thermal shock, should allow much more aggressive pumping of an AlN host without damaging the material.
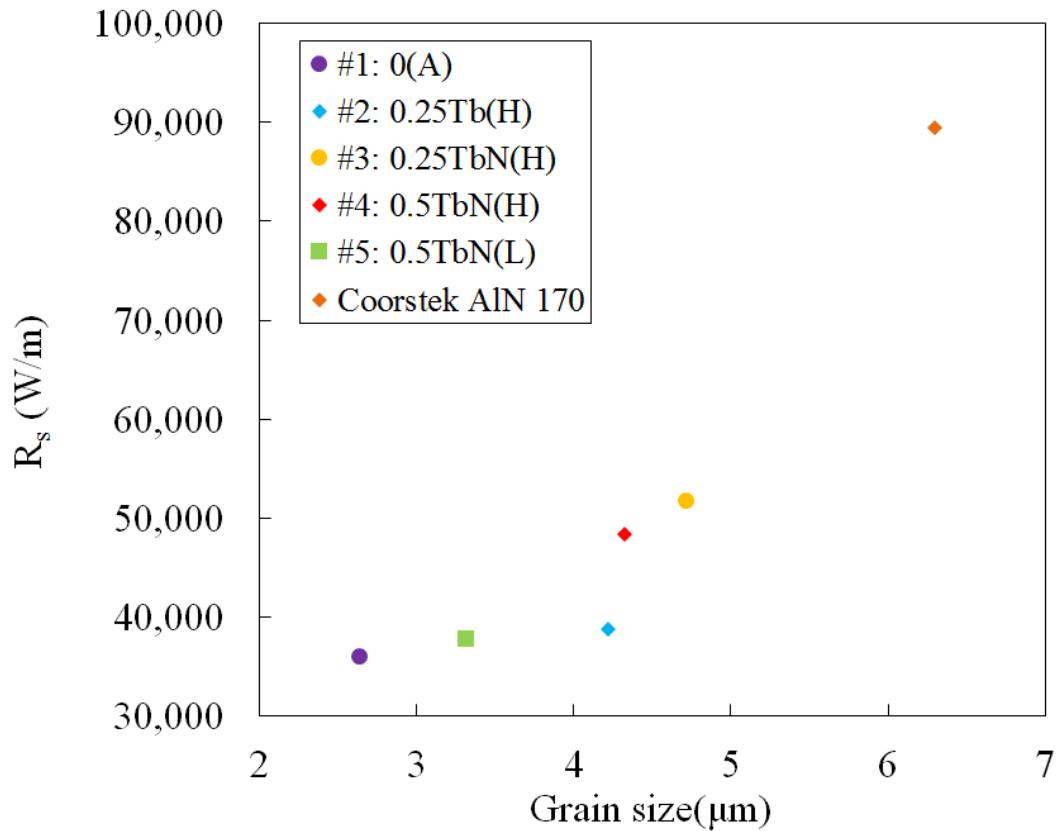

Figure 4.16 Thermal shock figure of merit as a function of grain size. Values of k measured at 310 K were used. [54]
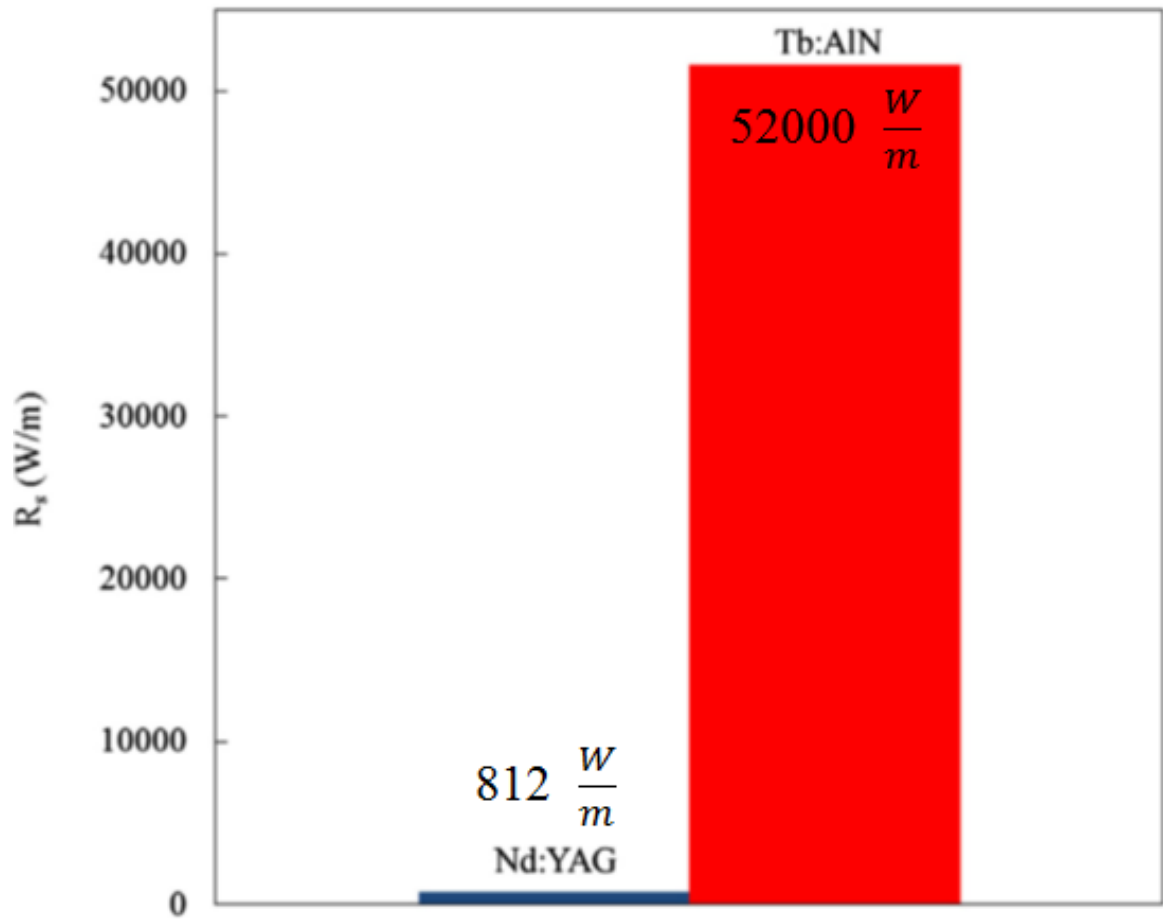
Figure 4.17 Comparison of thermal shock figure of merit (Rs) values calculated from measurements for single-crystal Nd:YAG and Tb:AlN (sample 4). [54]

5.0 Doping AlN for infrared emission

Neodymium has been shown to lase in an astonishing number of host materials and is a promising candidate for doping AlN. Laser light in the infrared (IR) region, especially the eye safe ~ 2 μm region has become increasingly popular for many applications including: remote sensing, communication, range finding and others. Demand and applications for these wavelengths is likely to continue to increase.

5.1 Neodymium (Nd) doped AlN microstructure

Neodymium doped AlN samples were characterized for microstructural uniformity as described in **Figure 3.2**, and it was found that the microstructure was very uniform within each sample and fairly similar between samples. **Figure 5.1** shows an example of the microstructural uniformity within a 0.5Nd:AlN sample (Nd1) at three different points on the same sample. While the sample shows some dopant segregation, the amount of segregation is quite uniform throughout the sample. **Figure 5.2** shows some of the microstructural differences observed between three different samples (Nd1,Nd2,Nd3) processed under the same conditions and as can be seen the microstructure was found to be fairly uniform between samples.

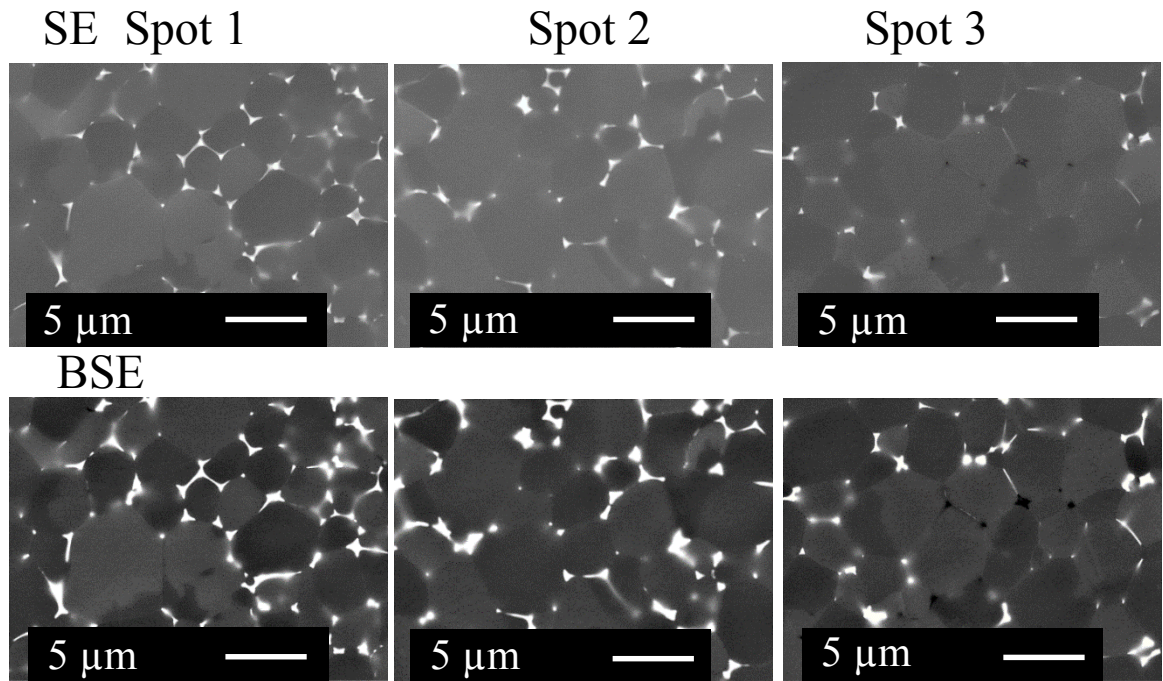SE Spot 1   Spot 2   Spot 3

BSE

Figure 5.1 Secondary and back scatter electron detector SEM micrographs of three different spots within sample Nd1 (**Table 2**), taken according to the procedure described in section **3.3**. These micrographs from different areas of the same sample demonstrate a high degree of microstructural uniformity within the sample.
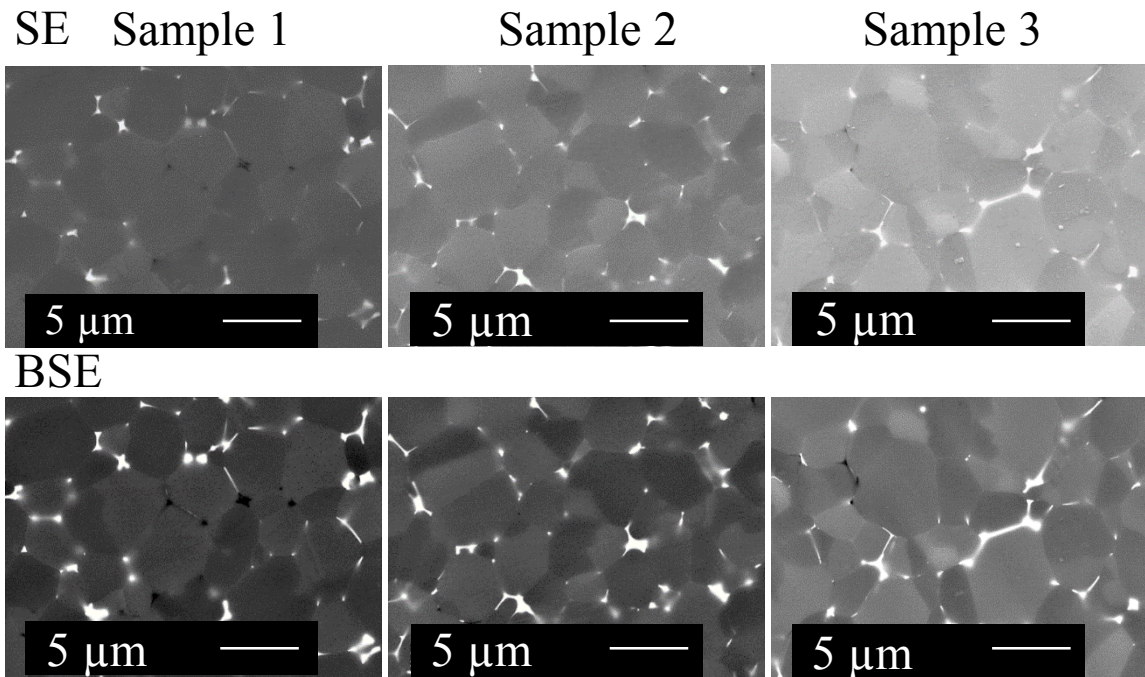
Figure 5.2 Evidence of microstructural uniformity between Nd:AlN samples. These secondary and back scatter electron detector SEM micrographs of three different spots each one in a different 0.5Nd:AlN sample (Nd1,Nd2,Nd3) as described in section **3.3**, show a high degree of microstructural uniformity between samples.

5.2 Nd doped AlN PL emission

Neodymium doped PL materials are typically excited with 808 nm light, and these samples are no exception. **Figure 5.3** shows an example of luminescence behavior observed in Nd:AlN under 808 nm excitation. Under closer examination it was observed that the structure of the observed photoluminescence peaks in Nd doped AlN changes based on the cleanliness of the grain boundaries. With increasing grain boundary cleanliness and thus likely an increase in crystallinity, the luminescence displays more sharp peaks than in samples with a higher degree of dopant segregation on the grain boundaries. An example of this luminescence-microstructure relationship is shown in **Figure 5.4**. Lorentzian peak fitting was conducted on the PL peaks presented in figure

5.4, these curves (green and red traces) are presented superimposed over the measured data (black trace). **Table 5** lists full with half max values for Lorentzian peak fits for Nd:Aln samples with clean and segregated grain boundaries.

If we compare the photoluminescence peaks observed in bulk polycrystalline Nd:AlN with the results observed in commercial samples of Nd:glass, and single crystal Nd:YAG as shown in **Figure 5.5** (a. Nd:glass, b. 0.5Nd:AlN and c.Nd:YAG) an interesting trend is observable. With increasing degree of crystallinity from amorphous glass to polycrystalline Nd:AlN to single crystal YAG, significant differences in the structure of the luminescence peaks are observed.

Looking first at commercial Nd:glass, a single fairly broad single peak at 1054 nm which corresponds well to the behavior of rare earth ions in an amorphous host. Following a trend of increasing crystallinity, 0.5Nd:AlN a bulk polycrystalline shows increased structure in the measured PL peaks as compared to Nd:glass, while single crystal Nd:YAG shows very clear sharp PL peaks. The photoluminescence emission measured in Nd:AlN falls quite neatly in between what was observed in an amorphous host material like Nd:glass and a highly crystalline material like single crystal Nd:YAG. This behavior makes sense since the samples made in this study while made from a crystalline material, are polycrystalline not single crystal. Their PL behavior falls right in between what is observed in an amorphous material and a single crystal host.

Because of the increase in photoluminescence intensity observed with annealing in Tb:AlN, a similar study was conducted in 0.5Nd:AlN. The resulting nearly 4 fold increase in intensity observed in this study is shown in Figure 5.6. The observed increase in intensity is likely due to an improvement in the crystalline environment from annealing, similar to the improvements observed from increasing host crystallinity.
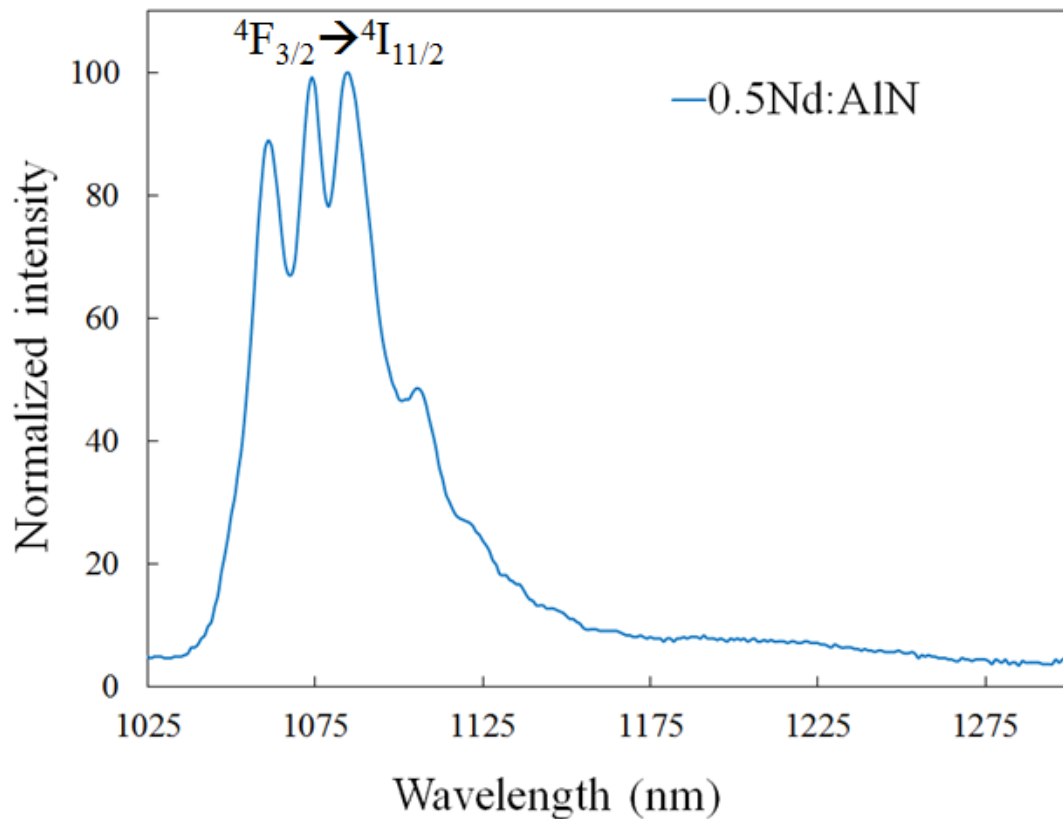
Figure 5.3 Luminescence behavior observed in 0.5Nd:AlN (Nd6) under 808 nm excitation. The peak shown here centered at 1075 nm is characteristic of the $^4F_{3/2} \rightarrow {}^4I_{11/2}$ transition in neodymium.
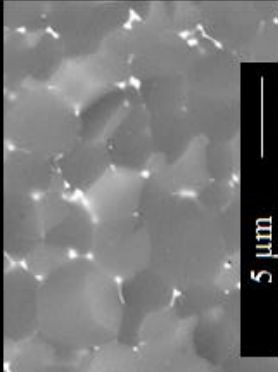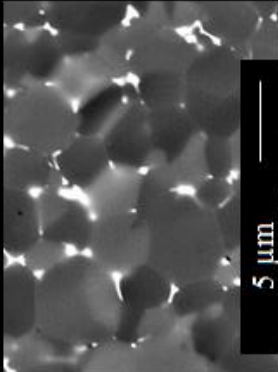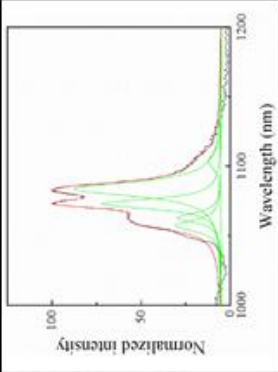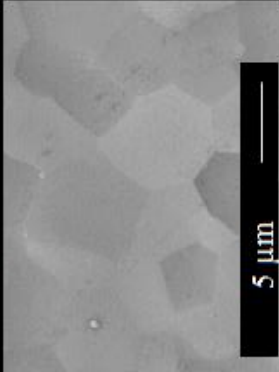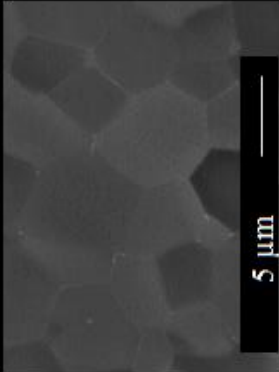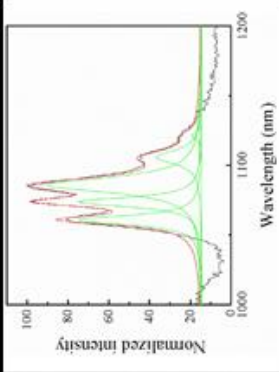
Figure 5.4 Secondary and back scatter detector SEM micrographs of samples Nd1 and Nd6 from **Table 2** showing examples of very clean and segregated grain boundaries (Nd6 and Nd1 respectively) (a) and corresponding PL measurements with Lorentzian peak fits for samples Nd1 and Nd6 (b). The full width half max (FWHM) values for the Lorentzian peaks shown here are presented in **Table 5**.

Peak location (nm)	FWHM clean grain boundaries (nm) Sample Nd6	Peak location (nm)	FWHM segregated grain boundaries (nm) Sample Nd1
1061	11	1057	12
1074	11	1063	11
1086	16	1073	10
1106	25	1084	13
1122	21	1104	24

Table 5 Peak locations and full width half max values from lorentzian peak fits on Nd:AlN samples with clean and segregated grain boundaries.
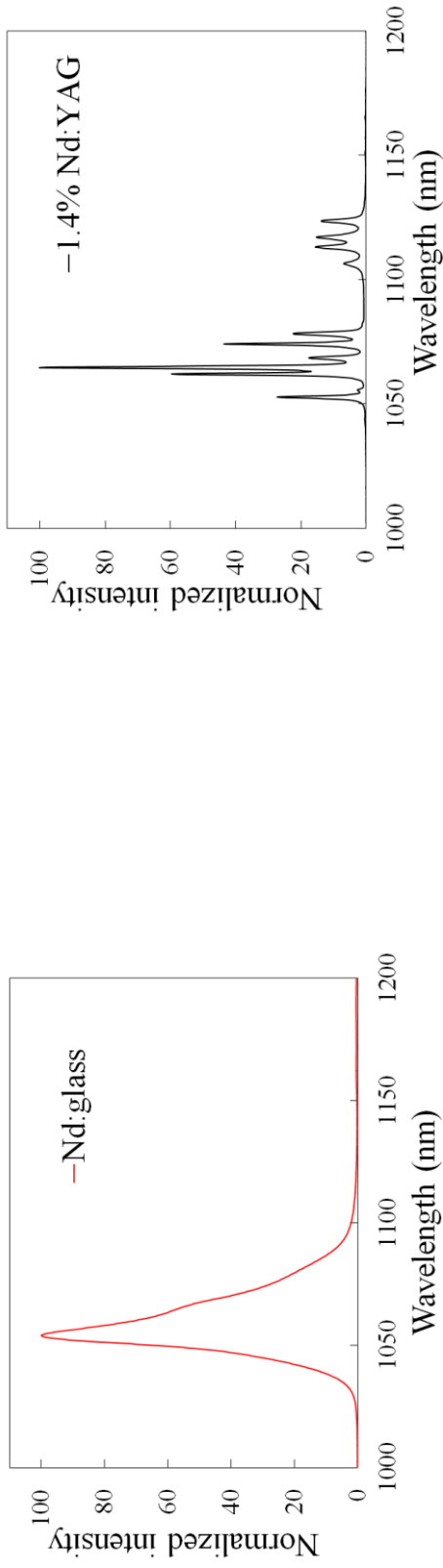
(a)Amorphous   (b)Polycrystalline   (c)Single crystal
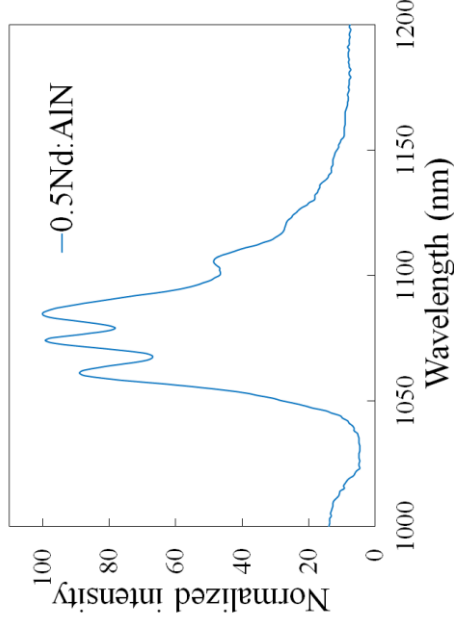
Figure 5.5 Comparison of Nd PL emission in different PL hosts, in order of increasing crystallinity (a) commercial Nd:glass, (b) bulk polycrystalline 0.5Nd:AlN (this work, Nd6) and commercial single crystal Nd:YAG. With increasing degree of crystallinity, more PL structure becomes visible.
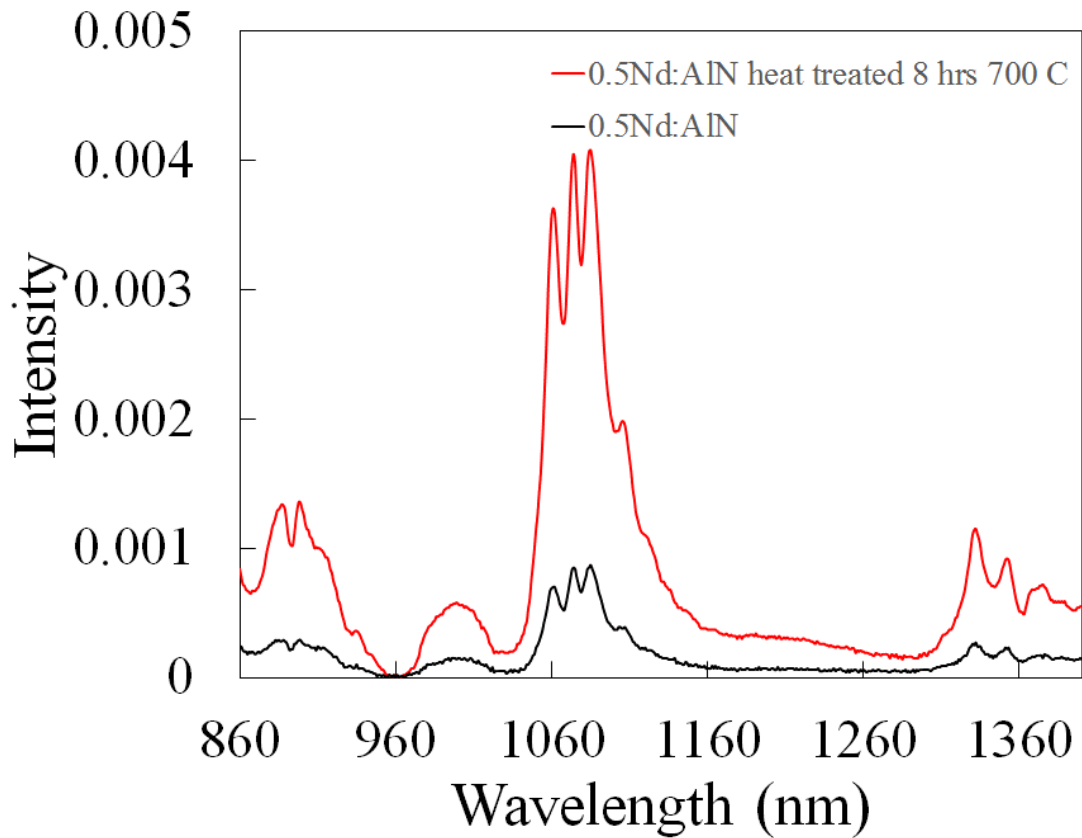
Figure 5.6 Improvement in PL intensity available in 0.5Nd:AlN (Nd6) from heat treating according to the procedure described in section **3.8** both Tb:AlN and Nd:AlN show improved PL intensity from this treatment. A 4.0 fold improvement was observed from annealing in 0.5Nd:AlN (Nd6)

Conclusions

By applying the ideas of non-equilibrium processing and combining highly energetic non-equilibrium processing techniques including high energy planetary ball milling and CAPAD processing, along with careful rare earth dopant source selection, significant progress has been made in the development of AlN as a high thermal conductivity PL host. Aluminum nitride was successfully densified to translucency without the use of sintering additives. Rare earth ions have been successfully doped into bulk polycrystalline AlN for both visible and infrared emission (Tb and Nd respectively) while achieving clean high quality microstructure. The PL intensity observed in bulk polycrystalline Tb:AlN and Nd:AlN was improved by nearly 2.5 and 4.0 fold respectively through annealing. A significant percentage of aluminum nitrides high thermal conductivity (94 $Wm^{-1}k^{-1}$) was retained in Tb doped AlN (sample 4). Because of its high thermal conductivity and good mechanical properties, a thermal shock resistance figure of merit for 0.5Tb:AlN that is 64 times higher than the current state of the art has been shown. Aluminum nitride shows significant promise as a high energy laser host material for the future.

References

[1]   Maiman, T. H. Stimulated Optical Radiation in Ruby. *Nature* **187**, 493-494 (1960).

[2]   Ikesue, A. & Aung, Y. L. Ceramic laser materials. *Nature photonics* **2**, 721-727 (2008).

[3]   Klein P. & Croft, W. Thermal Conductivity, Diffusivity, and Expansion of Y2O3, Y3Al5O12, and LaF3 in the Range 77- 300 K. *J. Appl. Phys.* **38**, 1603-1607 (1967).

[4]   Slack, G. A, Tanzilli, R. A, Pohl, R. O. & Vandersande J. W. The Intrinsic Thermal Conductivity of AlN. *J. Phys. Chem. Solids* **48**, 641-647 (1987).

[5]   Inoue, K, Hirosaki, N. , Xie, R. J. & Takeda, T. Highly Efficient and Thermally Stable Blue-Emitting AlN:Eu2+ Phosphor for Ultraviolet White Light-Emitting Diodes, *J. Phys. Chem. C* **113**, 9392-9397 (2009).

[6]   K. O'Donnell & V. Dierolf editors, Rare Earth Doped III-Nitrides for Optoelectronic and Spintronic Applications. Topics in Applied Physics Volume 124 (2010)

[7]   Torvik, J. T. *et al*. Electroluminescence from erbium and oxygen coimplanted GaN. *App. Phys. Lett.* **69**, 2098-2110 (1996).

[8]   Lee, D. S. & Steckl, A. J. Lateral color integration on rare-earth-doped GaN electroluminescent thin films. *App. Phys. Lett*. **80**, 1888-1890 (2002).

[9]   Steckl, A.J. , Heikenfeld, J. , Lee, D.S. & Garter, M. Multiple color capability from rare earth doped gallium nitride, *Mat. Sci. Eng. B* 81, 97–101 (2001).

[10] Lozykowskia, H. J, W.M. Jadwisienczaka, , Bensaoulab, A. & Monteiroc O. Luminescence and excitation mechanism of Pr, Eu, Tb and Tm ions implanted into AlN. *Microelectr. J.* **36**, 453–455 (2005).

[11] Weingartner, R. *et al*. Thermal activation, cathode- and photoluminescence measurements of rare earth doped (Tm. Tb, Dy, Eu, Sm, Yb) amorphous/nanocrystalline AlN thin films prepared by reactive rf-sputtering." *Opt. Mat.* **28**, 790-793 (2006).

[12] Garay, J. E. Current Activated Pressure Assisted Densification of Materials. *Annu. Rev. Mater. Res.* **40**, 445-468 (2010).

[13] Morales, J. R. , Amos, N. , Khizroev S. & Garay, J. E. Magneto-optical Faraday Effect in Nanocrystalline Oxides. *J. App. Phys.* **109**, 093110 (2011).

[14]   Alaniz, J. E. , Perez-Gutierrez, F. G. , Aguilar G. & Garay, J. E. Optical properties of transparent nanocrystalline yttria stabilized zirconia. *Opt. Mat.* **32**, 62-68 (2009).

[15] Casolco, S. R. , Xu J. & Garay, J. E. Transparent/translucent polycrystalline nanostructured yttria stabilized zirconia with varying colors. *Scripta Mater.* **58**, 516-519 (2008).

[16] Apetz R. & van Bruggen M. P. B. Transparent Alumina: A Light-Scattering Model. *J. Am. Ceram. Soc.* **86,** 480–486 (2003).

[17] Merkle, L. D. *et al.* Fluorescence of Er3+:AlN polycrystalline ceramic. *Opt. Mat. Exp.* 2, 78-90 (2012

[18] Qiao, L. , Zhou, H. & Li, C. Microstructure and thermal conductivity of spark

plasma sintering AlN ceramics. *Mat. Sci. Eng. B* **99**, 102-105 (2003).

[19]   Jackson, T. B. *et al*. High-thermal conductivity aluminum nitride ceramics: The effect of thermodynamic, kinetic, and microstructural factors. *J. Amer. Ceram. Soc.* **80**, 1421-1435 (1997).

[20]   Suryanarayana, C. Mechanical alloying and milling. *Prog. Mater. Sci.* **46**, 1-184 (2001).

[21]   Cox, G.A. , Cummins, D. O. , Kawabe, K. & Tredgold, R. H. On the preparation, optical properties and electrical behaviors of aluminum nitride. *J. Phys. Chem. Solids* **28**, 543-548 (1967).

[22]   Yim, W.M. *et al*. Epitaxially grown AlN and its optical band gap. *J. Appl. Phys.* **44**, 292-296 (1973).

[23]   Slack, G.A. & McNelly, T.F. Growth of high purity AlN crystals. *J. Crystal Growth* **34**. 263-279 (1976).

[24]   Dieke GH. 1968. Spectra and Energy Levels of Rare Earth Ions in Crystals, ed. HM Crosswhite, H Crosswhite. New York: Interscience

[25]   Li, J. *et al*. Fabrication, microstructure and properties of highly transparent Nd:YAG laser ceramics. *Opt. Mat.* **31**, 6-17(2008).

[26]   Cahill, D. G. Thermal conductivity measurement from 30 to 750 K: the 3 omega method. *Rev. Sci. Instrum.* **61**, 802-808 (1990).

[27]   Dames, C. Measuring the thermal conductivity of thin films: 3 omega and related electrothermal methods. *Annu. Rev.* Heat Transfer, (2012) (In revision).

[28]   Wang, Z. et al. Thermal Conductivity of Nanocrystalline Silicon: Importance of

Grain Size and Frequency-Dependent Mean Free Paths. Nano Letters **11**, 2206-2213 (2011).

[29] F. Karel, J Pastrnak. The Luminescence Properties of AlN With Manganese and Rare Earth Activators Under Ultraviolet and Cathode-Ray Excitation. Czech Journal of Physics B 20 (1970)

[30] M.P. Borom, G. A. Slack, J. W. Szymaszek. Thermal Conductivity of Commercial Aluminum Nitride. American Ceramics Society Bulletin 51 852-856 (1972).

[31] Tetsuo Matsumura, Yasaku Tanabe. Synthesis of AlN Crystals. Journal of the Physical Society of Japan 15 (1960) 203.

[32] J. Pastrnak and L. Roskovcova. Refraction Index Measurements on AlN Single Crystals. Physica Status Solidi 14 K5-K8 (1966)

[33] Fr. Karel, J. Pastrnak, J. Hejduk, V. Losik. Fine Structure of the Red AlN:Mn Luminescence. Physica Status Solidi 15 2 693-699 (1966)

[34] J. Pastrnak, S. Pacesova, L. Roskovcova. Luminescent properties of the Oxygen Impurity Centres in AlN. Czech. J. Phys. B 24 [1974]

[35] Jun-Kwang KIM and Woo-Sik JUNG. Nitridation of _-alumina to aluminum nitride under a flow of ammonia and its mechanism. Journal of the Ceramic Society of Japan 119 [5] 351-354 2011

[36] T. Suehiro, J. Tatami, T. Meguro, S. Matsuo, K. Komeya. Synthesis of spherical AlN particles by gas-reductionnitridation Method. Journal of the European Ceramic Society 22 (2002) 521–526

[37]   Iwama, Hayakawa and Arizumi. Journal of Crystal Growth 56 (1982) 265—269
        265

[38]   G. R. ANSTIS, P. CHANTIKUL, B. R. LAWN,* and D. B. MARSHALL. A
        Critical Evaluation of Indentation Techniques for Measuring Fracture Toughness:
        I, Direct Crack Measurements. JOURNAL OF THE AMERICAN CERAMIC
        SOCIETY Volume: 64 Issue: 9 Pages: 533-538 1981.

[39]   K. Niihara, R. Morena, D.P.H. Hasselman. Evaluation of 1Kic of brittle solids by
        the indentation method with low crack-to-indent ratios. Journal Of Materials
        Science Letters 1 (1982) 13-16

[40]   Koechner, Walter. Solid-State Laser Engineering. 2006, New York: Springer
        publishing

[41]   A. Ikesue, K. Kamata, K. Yoshida, J. Am. Ceram. Soc. 78 (1995) 225.

[42]   A. Ikesue, Yan Lin Aung , T. Yoda, S. Nakayama, T. Kamimura.
        Fabrication and laser performance of polycrystal and single crystal Nd:YAG by
        advanced ceramic processing. Optical Materials 29 (2007) 1289–1294

[43]   V. Lupei, A. Lupei, A. Ikesue. Transparent polycrystalline ceramic laser
        materials. Optical Materials 30 (2008) 1781–1786

[44]   V. Lupei, T. Taira, A. Lupei, N. Pavel, I. Shoji, A. Ikesue. Spectroscopy and laser
        emission under hot band resonant pump in highly doped Nd:YAG ceramics.
        Optics Communications 195 (2001) 225-232

[45]   Akio Ikesue and Yan Lin Aung. Ceramic laser materials. Nature Photonics 2 (2008) 721-727

[46]   W. M. Yim, E. J. Stofko, P. J. Zanzucchi, J. I. Pankove, M. Ettenberg, and S. L. Gilbert. Epitaxially grown AIN and its optical band gap. Journal of Applied Physics 44, 292 (1973) 292-296.

[47]   R. Terao, J. Tatami, T. Meguro, K. Komeya. Fracture behavior of AlN ceramics with rare earth oxides. Journal of the European Ceramic Society 22 (2002) 1051–1059

[48]   Xiulan He, Feng Ye, Haijiao Zhang, Zhiqiang Zhou. Study on microstructure and thermal conductivity of Spark Plasma Sintering AlN ceramics. Materials and Design 31 (2010) 4110–4115.

[49]   K. Watari, *et al.*, "Thermal conductivity of AIN ceramic with a very low amount of grain boundary phase at 4 to 1000 K," *Journal of materials research,* vol. 17, pp. 2940-2944, 2002.

[50]   Gerlich, D, Dole S.L., Slack G.A., Journal of Physics and Chemistry of Solids 47, 5(1986), 437-441.

 [51]   Y. Xiong, Z.Y. Fu, H. Wang, Y.C. Wang, Q.J. Zhang. Materials Science and Engineering B 123 (2005) 57–62

[52]   Y. Kodera, C.L. Hardin, J.E. Garay, Scr. Mater. 69 (2013) 149.

[53]   A. T. Wieg, Y. Kodera, Z. Wang, T. Imai, C. Dames, and J. E. Garay. Applied Physics Letters 101, 111903 (2012)

[54]   A.T. Wieg, Y. Kodera, Z. Wang, C. Dames and J.E. Garay, Acta Materialia 86
        (2015) 148–156